Astronomy & Astrophysics manuscript no. szcosmo2014
February 6, 2015

arXiv:1502.01597v1 [astro-ph.CO] 5 Feb 2015

Planck 2015 results. XXIV. Cosmology from Sunyaev-Zeldovich cluster counts

Planck Collaboration: P. A. R. Ade[92], N. Aghanim[65], M. Arnaud[79], M. Ashdown[75,6], J. Aumont[65], C. Baccigalupi[91], A. J. Banday[102,10], R. B. Barreiro[71], J. G. Bartlett[1,73], N. Bartolo[31,72], E. Battaner[104,105], R. Battye[74], K. Benabed[66,101], A. Benoît[63], A. Benoit-Lévy[25,66,101], J.-P. Bernard[102,10], M. Bersanelli[34,53], P. Bielewicz[102,10,91], A. Bonaldi[74], L. Bonavera[71], J. R. Bond[9], J. Borrill[15,96], F. R. Bouchet[66,94], M. Bucher[1], C. Burigana[52,32,54], R. C. Butler[52], E. Calabrese[99], J.-F. Cardoso[80,1,66], A. Catalano[81,78], A. Challinor[68,75,13], A. Chamballu[79,17,65], R.-R. Chary[62], H. C. Chiang[28,7], P. R. Christensen[88,38], S. Church[98], D. L. Clements[61], S. Colombi[66,101], L. P. L. Colombo[24,73], C. Combet[81], B. Comis[81], F. Couchot[76], A. Coulais[78], B. P. Crill[73,12], A. Curto[6,71], F. Cuttaia[52], L. Danese[91], R. D. Davies[74], R. J. Davis[74], P. de Bernardis[33], A. de Rosa[52], G. de Zotti[49,91], J. Delabrouille[1], F.-X. Désert[58], J. M. Diego[71], K. Dolag[103,85], H. Dole[65,64], S. Donzelli[53], O. Doré[73,12], M. Douspis[65], A. Ducout[66,61], X. Dupac[41], G. Efstathiou[68], F. Elsner[25,66,101], T. A. Enßlin[85], H. K. Eriksen[69], E. Falgarone[78], J. Fergusson[13], F. Finelli[52,54], O. Forni[102,10], M. Frailis[51], A. A. Fraisse[28], E. Franceschi[52], A. Frejsel[88], S. Galeotta[51], S. Galli[66], K. Ganga[1], M. Giard[102,10], Y. Giraud-Héraud[1], E. Gjerløw[69], J. González-Nuevo[71,91], K. M. Górski[73,106], S. Gratton[75,68], A. Gregorio[35,51,57], A. Gruppuso[52], J. E. Gudmundsson[28], F. K. Hansen[69], D. Hanson[86,73,9], D. L. Harrison[68,75], S. Henrot-Versillé[76], C. Hernández-Monteagudo[14,85], D. Herranz[71], S. R. Hildebrandt[73,12], E. Hivon[66,101], M. Hobson[6], W. A. Holmes[73], A. Hornstrup[18], W. Hovest[85], K. M. Huffenberger[26], G. Hurier[65], A. H. Jaffe[61], T. R. Jaffe[102,10], W. C. Jones[28], M. Juvela[27], E. Keihänen[27], R. Keskitalo[15], T. S. Kisner[83], R. Kneissl[40,8], J. Knoche[85], M. Kunz[19,65,3], H. Kurki-Suonio[27,47], G. Lagache[5,65], A. Lähteenmäki[2,47], J.-M. Lamarre[78], A. Lasenby[6,75], M. Lattanzi[32], C. R. Lawrence[73], R. Leonardi[41], J. Lesgourgues[100,90,77], F. Levrier[78], M. Liguori[31,72], P. B. Lilje[69], M. Linden-Vørnle[18], M. López-Caniego[41,71], P. M. Lubin[29], J. F. Macías-Pérez[81], G. Maggio[51], D. Maino[34,53], N. Mandolesi[52,32], A. Mangilli[65,76], P. G. Martin[9], E. Martínez-González[71], S. Masi[33], S. Matarrese[31,72,44], P. Mazzotta[36], P. McGehee[62], P. R. Meinhold[29], A. Melchiorri[33,55], J.-B. Melin[17], L. Mendes[41], A. Mennella[34,53], M. Migliaccio[68,75], S. Mitra[60,73], M.-A. Miville-Deschênes[65,9], A. Moneti[66], L. Montier[102,10], G. Morgante[52], D. Mortlock[61], A. Moss[93], D. Munshi[92], J. A. Murphy[87], P. Naselsky[88,38], F. Nati[28], P. Natoli[32,4,52], C. B. Netterfield[21], H. U. Nørgaard-Nielsen[18], F. Noviello[74], D. Novikov[84], I. Novikov[88,84], C. A. Oxborrow[18], F. Paci[91], L. Pagano[33,55], F. Pajot[65], D. Paoletti[52,54], B. Partridge[46], F. Pasian[51], G. Patanchon[1], T. J. Pearson[12,62], O. Perdereau[76], L. Perotto[81], F. Perrotta[91], V. Pettorino[45], F. Piacentini[33], M. Piat[1], E. Pierpaoli[24], D. Pietrobon[73], S. Plaszczynski[76], E. Pointecouteau[102,10], G. Polenta[4,50], L. Popa[67], G. W. Pratt[79], G. Prézeau[12,73], S. Prunet[66,101], J.-L. Puget[65], J. P. Rachen[22,85], R. Rebolo[70,16,39], M. Reinecke[85], M. Remazeilles[74,65,1], C. Renault[81], A. Renzi[37,56], I. Ristorcelli[102,10], G. Rocha[73,12], M. Roman[1], C. Rosset[1], M. Rossetti[34,53], G. Roudier[1,78,73], J. A. Rubiño-Martín[70,39], B. Rusholme[62], M. Sandri[52], D. Santos[81], M. Savelainen[27,47], G. Savini[89], D. Scott[23], M. D. Seiffert[73,12], E. P. S. Shellard[13], L. D. Spencer[92], V. Stolyarov[6,75,97], R. Stompor[1], R. Sudiwala[92], R. Sunyaev[85,95], D. Sutton[68,75], A.-S. Suur-Uski[27,47], J.-F. Sygnet[66], J. A. Tauber[42], L. Terenzi[43,52], L. Toffolatti[20,71,52], M. Tomasi[34,53], M. Tristram[76], M. Tucci[19], J. Tuovinen[11], M. Türler[59], G. Umana[48], L. Valenziano[52], J. Valiviita[27,47], B. Van Tent[82], P. Vielva[71], F. Villa[52], L. A. Wade[73], B. D. Wandelt[66,101,30], I. K. Wehus[73], J. Weller[103], S. D. M. White[85], D. Yvon[17], A. Zacchei[51], and A. Zonca[29]

(Affiliations can be found after the references)

Received ; accepted

ABSTRACT

We present cluster counts and corresponding cosmological constraints from the *Planck* full mission data set. Our catalogue consists of 439 clusters detected via their Sunyaev-Zeldovich (SZ) signal down to a signal-to-noise of six, and is more than a factor of two larger than the 2013 *Planck* cluster cosmology sample. The counts are consistent with those from 2013 and yield compatible constraints under the same modelling assumptions. Taking advantage of the larger catalogue, we extend our analysis to the two-dimensional distribution in redshift and signal-to-noise. We use mass estimates from two recent studies of gravitational lensing of background galaxies by Planck clusters to provide priors on the hydrostatic bias parameter, $1-b$. In addition, we use lensing of cosmic microwave background (CMB) temperature fluctuations by *Planck* clusters as a third independent constraint on this parameter. These various calibrations imply constraints on the present-day amplitude of matter fluctuations in varying degrees of tension with those coming from Planck analysis of primary fluctuations in the CMB; for the lowest estimated values of $1-b$ the tension is mild, only a little over one standard deviation, while for the largest estimated value it remains substantial. We also examine constraints on extensions to the base flat ΛCDM model by combining the cluster and CMB constraints. The combination appears to favour non-minimal neutrino masses, but this possibility does little to relieve the overall tension because it simultaneously lowers the implied value of the Hubble parameter, thereby exacerbating the discrepancy with most current astrophysical estimates. Improving the precision of cluster mass calibrations from the current 10%-level to 1% would significantly strengthen these combined analyses and provide a stringent test of the base ΛCDM model.

1. Introduction

Galaxy cluster counts are a standard cosmological tool that has found powerful application in recent Sunyaev-Zeldovich (SZ) surveys performed by the Atacama Cosmology Telescope (ACT, Swetz et al. 2011; Hasselfield et al. 2013), the South Pole Telescope (SPT, Carlstrom et al. 2011; Benson et al. 2013; Reichardt et al. 2013; Bocquet et al. 2014), and the *Planck* satellite[1] (Tauber et al. 2010; Planck Collaboration I 2011). The abun-

---

[1] *Planck* (`http://www.esa.int/Planck`) is a project of the European Space Agency (ESA) with instruments provided by two scientific consortia funded by ESA member states and led by Principal Investigators from France and Italy, telescope reflectors provided through a collaboration between ESA and a scientific consortium led and funded by Denmark, and additional contributions from NASA (USA).

dance of clusters and its evolution are sensitive to the cosmic matter density, $\Omega_{\rm m}$, and the present amplitude of density fluctuations, characterised by σ_8, the rms linear overdensity in spheres of radius $8h^{-1}$ Mpc. The primary cosmic microwave background (CMB) anisotropies, on the other hand, reflect the density perturbation power spectrum at the time of recombination. This difference is important because a comparison of the two tests the evolution of density perturbations from recombination until today, enabling us to look for possible extensions to the base ΛCDM model, such as non-minimal neutrino masses or non-zero curvature.

Launched on 14 May 2009, *Planck* scanned the entire sky twice a year from 12 August 2009 to 23 October 2013 at angular resolutions from 33′ to 5′with two instruments: the Low Frequency Instrument (LFI; Bersanelli et al. 2010; Mennella et al. 2011), covering bands centred at 30, 44, and 70 GHz, and the High Frequency Instrument (HFI; Lamarre et al. 2010; Planck HFI Core Team 2011), covering bands centred at 100, 143, 217, 353, 545, and 857 GHz.

A initial set of cosmology results appeared in 2013 based on the first 15.5 months of data (Planck Collaboration I 2014), including cosmological constraints from the redshift distribution of 189 galaxy clusters detected at signal-to-noise (SNR) > 7 (hereafter, our "first analysis" or the "2013 analysis", Planck Collaboration XX 2014). The present paper is part of the second set of cosmology results obtained from the full mission data set; it is based on an updated cluster sample introduced in an accompanying paper (the PSZ2, Planck Collaboration I 2015).

Our first analysis found fewer clusters than predicted by *Planck*'s base ΛCDM model, expressed as tension between the cluster constraints on $(\Omega_{\rm m}, \sigma_8)$ and those from the primary CMB anisotropies (Planck Collaboration XVI 2014). This could reflect the need for an extension to the base ΛCDM model, or indicate that clusters are more massive than determined by the SZ signal-mass scaling relation adopted in 2013.

The cluster mass scale is the largest source of uncertainty in interpretation of the cluster counts. We based our first analysis on X-ray mass proxies that rely on the assumption of hydrostatic equilibrium. Simulations demonstrate that this assumption can be violated by bulk motions in the gas or by nonthermal sources of pressure (e.g., magnetic fields or cosmic rays, Nagai et al. 2007; Piffaretti & Valdarnini 2008; Meneghetti et al. 2010). Systematics in the X-ray analyses (e.g., instrument calibration, temperature structure in the gas) could also bias the mass measurements significantly. We quantified our ignorance of the true mass scale of clusters with a mass bias parameter that was varied over the range [0 − 30]%, with a baseline value of 20% (see below for the definition of the mass bias), as suggested by numerical simulations (see the Appendix of Planck Collaboration XX 2014).

Gravitational lensing studies of the SZ signal-mass relation are particularly valuable in this context because they are independent of the dynamical state of the cluster (Marrone et al. 2012; Planck Collaboration Int. III 2013), although they also, of course, can be affected by systematic effects (e.g., Becker & Kravtsov 2011). New, more precise lensing mass measurements for *Planck* clusters have appeared since our 2013 analysis (von der Linden et al. 2014b; Hoekstra et al. 2015). We incorporate these new results as prior constraints on the mass bias in the present analysis. Two other improvements over 2013 are use of a larger cluster catalogue and analysis of the counts in signal-to-noise as well as redshift.

In addition, we apply a novel method to measure cluster masses through lensing of the CMB anisotropies. This method, presented in Melin & Bartlett (2014), enables us to use *Planck* data alone to constrain the cluster mass scale. It provides an important independent mass determination, which we compare to the galaxy lensing results, and one that is representative in the sense that it averages over the entire cluster cosmology sample, rather than a particularly chosen subsample.

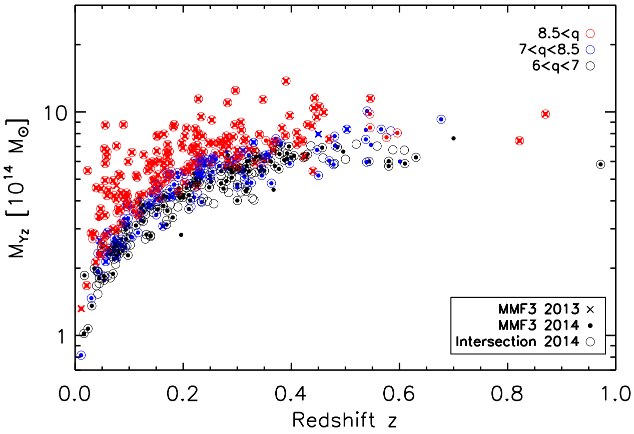

Fig. 1: Mass-redshift distribution of the *Planck* cosmological samples colour-coded by their signal-to-noise, q. The baseline MMF3 2015 cosmological sample is shown as the small filled circles. Objects which were in the MMF3 2013 cosmological sample are marked by crosses, while those in the 2015 intersection sample are shown as open circles. The final samples are defined by $q > 6$. The mass $M_{\rm Yz}$ is the *Planck* mass proxy (see text, Arnaud et al. 2015).

Our conventions throughout the paper are as follows. We specify cluster mass, M_{500}, as the total mass within a sphere of radius R_{500}, defined as the radius within which the mean mass over-density of the cluster is 500 times the cosmic critical density at its redshift, z: $M_{500} = (4\pi/3)R^3_{500}[500\rho_{\rm c}(z)]$, with $\rho_{\rm c}(z) = 3H^2(z)/(8\pi G)$, where $H(z)$ is the Hubble parameter with present-day value $H_0 = h \times 100$ km s^{-1} Mpc^{-1}. We give SZ signal strength, Y_{500}, in terms of the Compton y-profile integrated within a sphere of radius R_{500}, and we assume that all clusters follow the universal pressure profile of Arnaud et al. (2010). Density parameters are defined relative to the present-day critical density, e.g., $\Omega_{\rm m} = \rho_{\rm m}/\rho_{\rm c}(z = 0)$ for the total matter density, $\rho_{\rm m}$.

We begin in the next section with a presentation of the *Planck* 2015 cluster cosmology samples. In Sect. 3 we develop our model for the cluster counts in both redshift and signal-to-noise, including a discussion of the scaling relation, scatter and the sample selection function. Section 4 examines the overall cluster mass scale in light of recent gravitational lensing measurements; we also present our own calibration of the cluster mass scale based on lensing of the CMB temperature fluctuations. Construction of the cluster likelihood and selection of external data sets is detailed in Sect. 5. We present cosmological constraints in Sect. 6 and then summarize and discuss our results in Sect. 7. We examine the potential impact of different modeling uncertainties in the Appendix.

2. The *Planck* cosmological samples

We detect clusters across the six highest frequency Planck bands (100 − 857 GHz) using two implementations of the multifrequency matched filter (MMF3 and MMF1, Melin et al. 2006; Planck Collaboration XXIX 2014) and a Bayesian extension (PwS, Carvalho et al. 2009) that all incorporate the known (non-relativistic) SZ spectral signature and a model for the spatial profile of the signal. The latter is taken as the so-called universal pressure profile from Arnaud et al. (2010) — with the non standard self-similar scaling — and parameterized by an angular scale, θ_{500}.

We empirically characterize noise (all non-SZ signals) in localized sky patches (10° on a side for MMF3) using the set of cross-frequency power-spectra, we construct the filters with the resulting noise weights, and we then filter the set of six frequency maps over a range of cluster scales, θ_{500}, spanning 1–35 arcmin. The filter returns an estimate of Y_{500} for each scale, based on the adopted profile template, and sources are finally assigned the θ_{500} (and hence Y_{500}) of the scale that maximizes their signal-to-noise. Details are given in Planck Collaboration XXIX (2014) and in an accompanying paper introducing the *Planck* full-mission SZ catalogue (`PSZ2`, Planck Collaboration XXVII 2015).

We define two cosmological samples from the general `PSZ2` catalogues, one consisting of detections by the MMF3 matched filter and the other of objects detected by all three methods (the intersection catalogue). Both are defined by a signal-to-noise (denoted q throughout) cut of $q > 6$. We then apply a mask to remove regions of high dust emission and point sources, leaving 65% of the sky unmasked. The general catalogues, noise maps and masks can be downloaded from the Planck Legacy Archive[2].

The cosmological samples can be easily constructed from the `PSZ2` union and MMF3 catalogues. The MMF3 cosmology sample is the subsample of the MMF3 catalogue defined by $q > 6$ and for which the entry in the union catalogue has `COSMO`='T'. The intersection cosmology sample is defined from the union catalogue by the criteria `COSMO`='T', `PIPEDET`=111, and $q > 6$.

Fig. 1 shows the distribution of these samples in mass and redshift, together with the 2013 cosmology sample. The mass here is the *Planck* mass proxy, $M_{\rm Yz}$, defined in Arnaud et al. (2015) and taken from the `PSZ2` catalogue. It is calculated using the Planck size-flux posterior contours in conjunction with X-ray priors to break the size-flux degeneracy inherent to the large *Planck* beams (see, e.g. Fig. 16 of Planck Collaboration XXVII (2015)). The samples span masses in the range $[2-10]\times10^{14}\,M_\odot$ and redshifts from $z = 0$ to 1[3]. The MMF3 (intersection) sample contains 439 (493) detections. Note that the intersection catalogue has more objects than the MMF3 catalogue because of the different definitions of the signal-to-noise in the various catalogues. The signal-to-noise for the intersection catalogue corresponds to the highest signal-to-noise of the three detection algorithms (MMF1, MMF3 or PwS), while for the MMF3 catalogue we use its corresponding signal-to-noise. As a consequence, the lowest value for the MMF3 signal-to-noise in the intersection sample is 4.8. We note that, while being above our detection limit, the Virgo and the Perseus clusters are not part of our samples. This is because Virgo is too extended to be blindly detected by our algorithms and Perseus is close to a masked region.

The 2015 MMF3 cosmology sample contains all but one of the 189 clusters of the 2013 MMF3 sample. The missing cluster is PSZ1 980, which falls inside the 2015 point source mask. Six (14) redshifts are missing from the MMF3 (intersection) sample. Our analysis accounts for these by renormalizing the observed counts to redistribute the missing fraction uniformly across redshift. The small number of clusters with missing redshifts has no significant impact on our results.

We use the MMF3 cosmology sample at $q > 6$ for our baseline analysis and the intersection sample for consistency checks, as detailed in the Appendix. In particular, we show that the intersection sample yields equivalent constraints.

3. Modelling cluster counts

From the theoretical perspective, cluster abundance is a function of halo mass and redshift as specified by the mass function. Observationally, we detect clusters in *Planck* through their SZ signal strength or, equivalently, their signal-to-noise and measure their redshift with follow-up observations. The observed cluster counts are therefore a function of redshift, z, and signal-to-noise, q. While we restricted our 2013 cosmology analysis to the redshift distribution alone (Planck Collaboration XX 2014), the larger catalogue afforded by the full mission data set offers the possibility of an analysis in both redshift and signal-to-noise. We therefore develop the theory in terms of the joint distribution of clusters in the (z, q)-plane and then relate it to the more specific analysis of the redshift distribution to compare with our previous results.

3.1. Counts as a function of redshift and signal-to-noise

The distribution of clusters in redshift and and signal-to-noise can be written as

$$\frac{dN}{dzdq} = \int d\Omega_{\rm mask} \int dM_{500}\, \frac{dN}{dzdM_{500}d\Omega}\, P[q|\bar{q}_{\rm m}(M_{500}, z, l, b)], \tag{1}$$

with

$$\frac{dN}{dzdM_{500}d\Omega} = \frac{dN}{dVdM_{500}}\frac{dV}{dzd\Omega}, \tag{2}$$

i.e., the dark matter halo mass function times the volume element. We adopt the mass function from Tinker et al. (2008) throughout, apart from the Appendix where we compare to the Watson et al. (2013) mass function as a test of modelling robustness; there, we show that the Watson et al. (2013) mass function yields constraints similar to those from the Tinker et al. (2008) mass function, but shifted by about 1σ towards higher Ω_m and lower σ_8 along the main degeneracy line.

The quantity $P[q|\bar{q}_{\rm m}(M_{500}, z, l, b)]$ is the distribution of q given the mean signal-to-noise value, $\bar{q}_{\rm m}(M_{500}, z, l, b)$, predicted by the model for a cluster of mass M_{500} and redshift z located at Galactic coordinates (l, b)[4]. This latter quantity is defined as the ratio of the mean SZ signal expected of a cluster, $\bar{Y}_{500}(M_{500}, z)$, as given in Eq. (7), and the detection filter noise, $\sigma_{\rm f}[\bar{\theta}_{500}(M_{500}, z), l, b]$:

$$\bar{q}_{\rm m} \equiv \bar{Y}_{500}(M_{500}, z)/\sigma_{\rm f}[\bar{\theta}_{500}(M_{500}, z), l, b]. \tag{3}$$

The filter noise depends on sky location (l, b) and the cluster angular size, $\bar{\theta}_{500}$, which introduces additional dependence on mass and redshift. More detail on $\sigma_{\rm f}$ can be found in Planck Collaboration XX (2014) (see in particular Fig. 4 therein).

The distribution $P[q|\bar{q}_{\rm m}]$ incorporates noise fluctuations and intrinsic scatter in the actual cluster Y_{500} around the mean value,

---

[2] http://pla.esac.esa.int/pla/aio/planckProducts.html

[3] We fix $h = 0.7$ and $\Omega_\Lambda = 1 - \Omega_{\rm m} = 0.7$ for the mass calculation.

[4] Note that this form assumes, as we do throughout, that the distribution depends on z and M_{500} only through the mean value $\bar{q}_{\rm m}$; specifically, that the intrinsic scatter, $\sigma_{\ln Y}$, of Eq. (9) is constant.

$\bar{Y}_{500}(M_{500}, z)$, predicted from the scaling relation. We discuss this scaling relation and our log-normal model for the intrinsic scatter below, and Sect. 4 examines the calibration of the overall mass scale for the scaling relation.

The redshift distribution of clusters detected at $q > q_{\rm cat}$ is the integral of Eq. (1) over signal-to-noise,

$$\begin{aligned} \frac{dN}{dz}(q > q_{\rm cat}) &= \int_{q_{\rm cat}}^{\infty} dq\, \frac{dN}{dzdq} \\ &= \int d\Omega \int dM_{500}\, \hat{\chi}(M_{500}, z, l, b)\, \frac{dN}{dzdM_{500}d\Omega}, \end{aligned} \quad (4)$$

with

$$\hat{\chi}(M_{500}, z, l, b) = \int_{q_{\rm cat}}^{\infty} dq\, P[q|\bar{q}_{\rm m}(M_{500}, z, l, b)]. \quad (5)$$

Equation (4) is equivalent to the expression used in our 2013 analysis if we write it in the form

$$\hat{\chi} = \int d\ln Y_{500} \int d\theta_{500} P(\ln Y_{500}, \theta_{500}|z, M_{500})\, \chi(Y_{500}, \theta_{500}, l, b), \quad (6)$$

where $\chi(Y_{500}, \theta_{500}, l, b)$ is the survey selection function at $q > q_{\rm cat}$ in terms of true cluster parameters (Sect. 3.3), and $P(\ln Y_{500}, \theta_{500}|z, M_{500})$ is the distribution of these parameters given cluster mass and redshift. We specify the relation between Eq. (5) and Eq. (6) in the next section.

3.2. Observable-mass relations

A crucial element of our modelling is the relation between cluster observables, Y_{500} and θ_{500}, and halo mass and redshift. Due to intrinsic variations in cluster properties, this relation is described by a distribution function, $P(\ln Y_{500}, \theta_{500}|M_{500}, z)$, whose mean values are specified by the scaling relations $\bar{Y}_{500}(M_{500}, z)$ and $\bar{\theta}_{500}(M_{500}, z)$.

We use the same form for these scaling relations as in our 2013 analysis:

$$E^{-\beta}(z)\left[\frac{D_{\rm A}^2(z)\bar{Y}_{500}}{10^{-4}\,{\rm Mpc}^2}\right] = Y_*\left[\frac{h}{0.7}\right]^{-2+\alpha}\left[\frac{(1-b)\,M_{500}}{6\times 10^{14}\,{\rm M}_\odot}\right]^{\alpha}, \quad (7)$$

and

$$\bar{\theta}_{500} = \theta_*\left[\frac{h}{0.7}\right]^{-2/3}\left[\frac{(1-b)\,M_{500}}{3\times 10^{14}{\rm M}_\odot}\right]^{1/3} E^{-2/3}(z)\left[\frac{D_{\rm A}(z)}{500\,{\rm Mpc}}\right]^{-1}, \quad (8)$$

where $\theta_* = 6.997$ arcmin, and fiducial ranges for the parameters Y_*, α, and β are listed in Table 1; these values are identical to those used in our 2013 analysis. Unless otherwise stated, we use Gaussian distributions with mean and standard deviation given by these values as prior constraints; one notable exception will be when we simultaneously fit for α and cosmological parameters. In the above expressions, $D_{\rm A}(z)$ is the angular diameter distance and $E(z) \equiv H(z)/H_0$.

These scaling relations have been established by X-ray observations, as detailed in the Appendix of Planck Collaboration XX (2014), and rely on mass determinations, $M_{\rm X}$, based on hydrostatic equilibrium of the intra-cluster gas. The *mass bias* parameter, b, assumed to be constant in both mass and redshift, allows for any difference between the X-ray determined masses and true cluster halo mass: $M_{\rm X} = (1-b)M_{500}$. This is discussed at length in Sect. 4.

Table 1: Summary of SZ-mass scaling law parameters (see Eq. 7).

Parameter	Value
$\log Y_*$	-0.19 ± 0.02
α[a]	1.79 ± 0.08
β[b]	0.66 ± 0.50
$\sigma_{\ln Y}$[c]	0.127 ± 0.023

[a] Except when specified, α is constrained by this prior in our one-dimensional likelihood over $N(z)$, but left free in our two-dimensional likelihood over $N(z, q)$.

[b] We fix β to its central value throughout, except when examining modelling uncertainties in the Appendix.

[c] The value is the same as in our 2013 analysis, given here in terms of the natural logarithm and computed from $\sigma_{\log Y} = 0.075 \pm 0.01$.

We adopt a log-normal distribution for Y_{500} around its mean value $\bar{Y}_{500}$, and a delta function for θ_{500} centred on $\bar{\theta}_{500}$:

$$\begin{aligned} P(\ln Y_{500}, \theta_{500}|M_{500}, z) &= \frac{1}{\sqrt{2\pi}\sigma_{\rm lnY}} e^{-\ln^2(Y_{500}/\bar{Y}_{500})/(2\sigma^2_{\rm lnY})} \\ &\times\ \delta[\theta_{500} - \bar{\theta}_{500}], \end{aligned} \quad (9)$$

where $\bar{Y}_{500}(M_{500}, z)$ and $\bar{\theta}_{500}(M_{500}, z)$ are given by Eqs. (7) and (8)[5] The δ-function maintains the empirical definition of R_{500} that is used in observational determination of the the profile.

We can now specify the relation between Eqs. (5) and (6) by noting that

$$P[q|\bar{q}_{\rm m}(M_{500}, z, l, b)] = \int d\ln q_{\rm m} P[q|q_{\rm m}] P[\ln q_{\rm m}|\bar{q}_{\rm m}], \quad (10)$$

where $P[q|q_{\rm m}]$ is the distribution of observed signal-to-noise, q, given the model value, $q_{\rm m}$. The second distribution represents intrinsic cluster scatter, which we write in terms of our observable-mass distribution, Eq. (9), as

$$\begin{aligned} P[\ln q_{\rm m}|\bar{q}_{\rm m}] &= \int d\theta_{500} P[\ln Y_{500}(\ln q_{\rm m}, \theta_{500}, l, b), \theta_{500}|M_{500}, z] \\ &= \frac{1}{\sqrt{2\pi}\sigma_{\rm lnY}} e^{-\ln^2(q_{\rm m}/\bar{q}_{\rm m})/2\sigma^2_{\rm lnY}}. \end{aligned} \quad (11)$$

Performing the integral of Eq. (5), we find

$$\hat{\chi} = \int d\ln q_{\rm m} P[\ln q_{\rm m}|\bar{q}_{\rm m}]\, \chi(Y_{500}, \theta_{500}, l, b), \quad (12)$$

with the definition of our survey selection function

$$\chi(Y_{500}, \theta_{500}, l, b) = \int_{q_{\rm cat}}^{\infty} dq P[q|q_{\rm m}(Y_{500}, \theta_{500}, l, b)]. \quad (13)$$

We then reproduce Eq. (6) by using the first line of Eq. (11) and Eq. (3).

3.3. Selection function and survey completeness

The fundamental quantity describing the survey selection is $P[q|q_{\rm m}]$, introduced in Eq. (10). It gives the observed signal-to-noise, used to select SZ sources, as a function of model ("true") cluster parameters through $q_{\rm m}(Y_{500}, \theta_{500}, l, b)$, and it defines the

---

[5] In this paper, 'ln' denotes the natural logarithm and 'log' the logarithm to base 10; the expression is written in terms of the natural logarithm.

survey selection function $\chi(Y_{500}, \theta_{500}, l, b)$ via Eq. (13). We characterize the survey selection in two ways. The first is with an analytical model and the second employs a Monte Carlo extraction of simulated sources injected into the *Planck* maps. In addition, we perform an external validation of our selection function using known X-ray clusters.

The analytical model assumes pure Gaussian noise, in which case we simply have $P[q|q_{\rm m}] = e^{-(q-q_{\rm m})^2/2}/\sqrt{2\pi}$. The survey selection function is then given by the Error Function (ERF),

$$\chi(Y_{500}, \theta_{500}, l, b) = \frac{1}{2}\left[1 - {\rm erf}\left(\frac{q_{\rm cat} - q_{\rm m}(Y_{500}, \theta_{500}, l, b)}{\sqrt{2}}\right)\right]. \quad (14)$$

This model can be applied to a catalogue with well-defined noise properties, i.e., $\sigma_{\rm f}$, such as our MMF3 catalogue, but not to the intersection catalogue based on the simultaneous detection with three different methods. This is our motivation for choosing the MMF3 catalogue as our baseline.

In the Monte Carlo approach, we inject simulated clusters directly into the *Planck* maps and (re)extract them with the complete detection pipeline. Details are given in the accompanying 2015 SZ catalogue paper, Planck Collaboration XXVII (2015). This method provides a more comprehensive description of the survey selection by accounting for a variety of effects beyond noise. In particular, we vary the shape of the SZ profile at fixed Y_{500} and θ_{500} to quantify its effect on catalogue completeness.

We also perform an external check of the survey completeness using known X-ray clusters from the MCXC compilation (Piffaretti et al. 2011) and also SPT clusters from Bleem et al. (2014). Details are given in the 2015 SZ catalogue paper, Planck Collaboration XXVII (2015). For the MCXC compilation, we rely on the expectation that at redshifts $z < 0.2$ any *Planck*-detected cluster should be found in one of the ROSAT catalogues (Chamballu et al. 2012), because at low redshift ROSAT probes to lower masses than *Planck*[6]. The MCXC catalogue provides a truth table, replacing the input cluster list of the simulations, and we compute completeness as the ratio of objects in the cosmology catalogue to the total number of clusters. As discussed in Planck Collaboration XXVII (2015), the results are consistent with Gaussian noise and bound the possible effect of profile variations. We arrive at the same conclusion when applying the technique to the SPT catalogue.

Planck Collaboration XXVII (2015) discusses completeness checks in greater detail. One possible source of bias is the presence of correlated IR emission from cluster member galaxies. Planck Collaboration XXIII (2015) suggests that IR point sources may contribute significantly to the cluster SED at the Planck frequencies, especially at higher redshift. The potential impact of this effect warrants further study in future work.

This gives us different estimations of the selection function for MMF3 and the intersection catalogues. We test the sensitivity of our cosmological constraints to the selection function in the Appendix by comparing results obtained with the different methods and catalogues. We find that our results are insensitive to the choice of completeness model (Fig A.1), and we therefore adopt the analytical ERF completeness function for simplicity throughout the paper.

4. The cluster mass scale

The characteristic mass scale of our cluster sample is the critical element in our analysis of the counts. It is controlled by the mass bias factor, $1-b$, accounting for any difference between the X-ray mass proxies used to establish the scaling relations and the true (halo) mass: $M_{\rm X} = (1-b)M_{500}$. Such a difference could arise from cluster physics, such as a violation of hydrostatic equilibrium or temperature structure in the gas, from observational effects, e.g., instrumental calibration, or from selection effects biasing the X-ray samples relative to SZ- or mass-selected samples (Angulo et al. 2012).

In our 2013 analysis, we adopted a flat prior on the mass bias over the range $1-b = [0.7, 1.0]$, with a reference model defined by $1-b = 0.8$. This was motivated by a comparison of the $Y-M_{\rm X}$ relation with published $Y-M$ relations derived from numerical simulations, as detailed in the Appendix of Planck Collaboration XX (2014); this estimate was consistent with most predictions for any violation of hydrostatic equilibrium (although not all) as well as observational constraints from the available lensing observations. Effects other than cluster physics can contribute to the mass bias, as discussed in the paper, and as emphasized by the survey of cluster multi-band scaling relations by Rozo et al. (2014a,b,c).

The mass bias was the largest uncertainty in our 2013 analysis, and it severely hampered understanding of the tension found between constraints from the primary CMB and the cluster counts. Here, we incorporate new lensing mass determinations of *Planck* clusters to constrain the mass bias. We also apply a novel method to measure object mass based on lensing of CMB temperature anisotropies behind clusters (Melin & Bartlett 2014). These constraints are used as prior information in our analysis of the counts. As we will see, however, uncertainty in the mass bias remains our largest source of uncertainty, mainly because these various determinations continue to differ from 10 to 30%.

In general, the mass bias could depend on cluster mass and redshift, although we will model it by a constant in the following. Our motivation is one of practicality: the limited size and precision of current lensing samples makes it difficult to constrain any more than a constant, i.e., the overall mass scale of our catalogue. Large lensing surveys like *Euclid*, WFIRST, and the Large Synoptic Survey Telescope, and CMB lensing will improve this situation in coming years.

4.1. Constraints from gravitational shear

Several cluster samples with high quality gravitational shear mass measurements have appeared since 2013. Among these, the Weighing the Giants (WtG, von der Linden et al. 2014a), CLASH (Postman et al. 2012; Merten et al. 2014; Umetsu et al. 2014), and the Canadian Cluster Comparison Project (CCCP, Hoekstra et al. 2015) programmes offer constraints on our mass bias factor, $1-b$, through direct comparison of the lensing masses to the *Planck* mass proxy, $M_{\rm Yz}$.

The analysis by the WtG programme of 22 clusters from the 2013 *Planck* cosmology sample yields $1-b = 0.688 \pm 0.072$. Their result lies at the very extreme of the range explored in Planck Collaboration XX (2014) and would substantially reduce the tension found between primary CMB and galaxy cluster constraints. Hoekstra et al. (2015) report a smaller bias of $1-b = 0.78 \pm 0.07$ (stat) ± 0.06 (sys) for a set of 20 common clusters, which is in good agreement with the fiducial value adopted in our 2013 analysis. In our analysis we add the statistical and systematic uncertainties in quadrature (see Table 2).

---

[6] In fact, this expectation is violated to a small degree. As discussed in Planck Collaboration XXVII (2015), there appears to be a small population of X-ray under-luminous clusters.

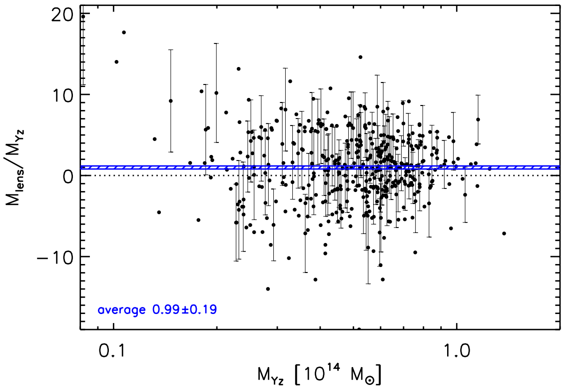

Fig. 2: The cluster mass scale determined by CMB lensing. We show the ratio of cluster lensing mass, $M_{\rm lens}$, to the SZ mass proxy, $M_{\rm Yz}$, as a function of the mass proxy for clusters in the MMF3 2015 cosmology sample. The cluster mass is measured through lensing of CMB temperature anisotropies in the *Planck* data (Melin & Bartlett 2014). Individual mass measurements have low signal-to-noise, but we determine a mean ratio for the sample of $M_{\rm lens}/M_{\rm Yz} = 1/(1-b) = 0.99 \pm 0.19$. For clarity, only a fraction of the error bars are plotted (see text).

Table 2: Summary of mass scale priors

Prior name	Quantity	Value & Gaussian errors
Weighing the Giants (WtG)	$1-b$	0.688 ± 0.072
Canadian Cluster Comparison Project (CCCP)	$1-b$	0.780 ± 0.092
CMB lensing (LENS)	$1/(1-b)$	0.99 ± 0.19
Baseline 2013	$1-b$	$0.8\,[-0.1,+0.2]$

Notes. CMB lensing directly measures $1/(1-b)$, which we implement in our analysis; purely for reference, that constraint translates approximately to $1-b = 1.01^{+0.24}_{-0.16}$. The last line shows the 2013 baseline — a reference model defined by $1-b = 0.8$ with a flat prior in the [0.7, 1] range.

4.2. Constraints from CMB lensing

Measuring cluster mass through CMB lensing has been discussed in the literature for some time since the study performed by Zaldarriaga & Seljak (1999) (see also Lewis & Challinor 2006). We apply a new technique for measuring cluster masses through lensing of CMB temperature anisotropies (Melin & Bartlett 2014), allowing us to calibrate the scaling relations using only *Planck* data. This is a valuable alternative to the galaxy lensing observations because it is independent and affected by different possible systematics. Additionally, we can apply it to the entire cluster sample to obtain a mass calibration representative of an SZ flux selected sample. Similar approaches using CMB lensing to measure halo masses were recently applied by SPT (Baxter et al. 2014) and ACT (Madhavacheril et al. 2014).

Our method first extracts a clean CMB temperature map with a constrained internal linear combination (ILC) of the *Planck* frequency channels in the region around each cluster; the ILC is constrained to nullify the SZ signal from the clusters themselves and provide a clean CMB map of 5 arcmin resolution. Using a quadratic estimator on the CMB map, we reconstruct the lensing potential in the field and then filter it to obtain an estimate of the cluster mass. The filter is an NFW profile (Navarro et al. 1997) with scale radius set by the *Planck* mass proxy for each cluster, and designed to return an estimate of the ratio $M_{\rm lens}/M_{\rm Yz}$, where $M_{\rm Yz}$ is the *Planck* SZ mass proxy. These individual measurements are corrected for any mean-field bias by subtracting identical filter measurements on blank fields; this accounts for effects of apodization over the cluster fields and correlated noise. The technique has been tested on realistic simulations of *Planck* frequency maps. More detail can be found in Melin & Bartlett (2014).

Figure 2 shows $M_{\rm lens}/M_{\rm Yz}$ as a function of $M_{\rm Yz}$ for all clusters in the MMF3 cosmology sample. Each point is an individual cluster[7]. For clarity, only some of the error bars on the ratio are shown; the error bars vary from 1.8 at the high mass end to 8.5 at the low mass end with a median of 4.2. There is no indication of a correlation between the ratio and $M_{\rm Yz}$, and we therefore fit for a constant ratio of $M_{\rm lens}/M_{\rm Yz}$ by taking the weighted mean (using the individual measurement uncertainties as provided by the filter) over the full data set. If the ratio differs from unity, we apply a correction to account for the fact that our filter aperture was not perfectly matched to the clusters. The correction is calculated assuming an NFW profile and is the order of a percent.

The final result is $1/(1-b) = 0.99 \pm 0.19$, traced by the blue band in the figure. Note that the method constrains $1/(1-b)$ rather than $1-b$ as in the case of the shear measurements. The calculated uncertainty on the weighted mean is consistent with a bootstrap analysis where we create new catalogues of the same size as the original by sampling objects from the original catalogue with replacement; the uncertainty from the bootstrap is then taken as the standard deviation of the bootstrap means.

4.3. Summary

The three mass bias priors are summarized in Table 2, and we will compare cosmological constraints obtained from each. We will assume Gaussian distributions for $1-b$ (gravitational shear) or $1/(1-b)$ (CMB lensing) with standard deviations given by the error column. We favour these three lensing results because of their direct comparison to the *Planck* mass proxy.

5. Analysis methodology

5.1. Likelihood

Our 2013 analysis employed a likelihood built on the cluster redshift distribution, dN/dz. With the larger 2015 catalogue, our baseline likelihood is now constructed on counts in the (z,q)-plane. We divide the catalogue into bins of size $\Delta z = 0.1$ (10 bins) and $\Delta \log q = 0.25$ (5 bins), each with an observed number $N(z_i, q_j) = N_{ij}$ of clusters. Modelling the observed counts, N_{ij}, as independent Poisson random variables, our log-likelihood is

$$\ln L = \sum_{i,j}^{N_z N_q} \left[N_{ij} \ln \bar{N}_{ij} - \bar{N}_{ij} - \ln[N_{ij}!] \right], \tag{15}$$

where N_z and N_q are the total number of redshift and signal-to-noise bins, respectively. The mean number of objects in each bin is predicted by theory according to Eq. (1):

$$\bar{N}_{ij} = \frac{dN}{dzdq}(z_i, q_j)\Delta z \Delta q, \tag{16}$$

---

[7] The values can be negative due to noise fluctuations and the low signal-to-noise of the individual measurements.

which depends on the cosmological (and cluster modelling) parameters. In practice, we use a Monte Carlo Markov chain (MCMC) to map the likelihood surface around the maximum and establish confidence limits.

Eq. (15) assumes the bins are uncorrelated, while a more complete description would include correlations due to large-scale clustering. In practice, our cluster sample contains mostly high mass systems for which the impact of these effects is weak (e.g., Hu & Kravtsov 2003, in particular their Fig. 4 for the impact on constraints in the (Ω_m,σ_8) plane).

5.2. External data sets

Cluster counts cannot constrain all pertinent cosmological parameters. They are most sensitive to $\Omega_{\rm m}$ and σ_8, and when analysing the counts alone we must apply additional observational constraints as priors on other parameters. For this purpose, we adopt Big Bang nucleosynthesis (BBN) constraints from Steigman (2008), $\Omega_b h^2 = 0.022 \pm 0.002$, and constraints from baryon acoustic oscillations (BAO). The latter combine the 6dF Galaxy Survey (Beutler et al. 2011), the SDSS Main Galaxy Sample (Padmanabhan et al. 2012; Anderson et al. 2012) and the BOSS DR11 (Anderson et al. 2014). We refer the reader to Sect. 5.2 in Planck Collaboration XIII (2015) for details of the combination. We also include a prior on n_s from Planck Collaboration XVI (2014), $n_s = 0.9624 \pm 0.014$. When explicitly specified in the text, we add the supernovæ constraint from SNLS-II and SNLS3: the Joint Light-curve Analysis constraint (JLA, Betoule et al. 2014). The BAO are particularly sensitive to H_0, while the supernovæ allow precise constraints on the dark energy equation-of-state parameter, w.

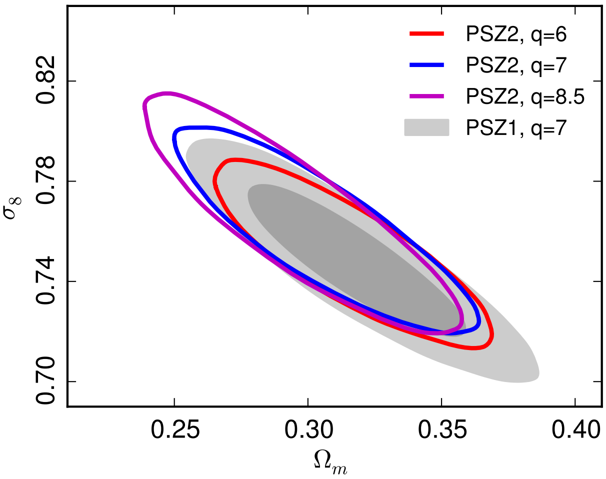

Fig. 3: Contours at 2σ for different signal-to-noise thresholds, $q = 8.5$, 7, and 6, applied to the 2015 MMF3 cosmology sample for the SZ+BAO+BBN data set. The contours are compatible with the 2013 constraints (Planck Collaboration XX 2014), shown as the filled, light grey ellipses at 1 and 2σ (for the BAO and BBN priors of Sect 5.2; see text). The 2015 catalogue thresholded at $q > 8.5$ has a similar number of clusters (190) as the 2013 catalogue (189). This comparison is made using the analytical error-function model for completeness and adopts the reference observable-mass scaling relation of the 2013 analysis [$1 - b = 0.8$, see text]. The redshift distributions of the best-fit models are shown in Fig. 4. For this figure and Fig. 4, we use the one-dimensional likelihood over the redshift distribution, dN/dz (Eq. 4).

6. Cosmological constraints

We begin by verifying consistency with the results of Planck Collaboration XX (2014) (Sect. 6.1) based on the one-dimensional likelihood over the redshift distribution, dN/dz (Eq. 4). We then examine the effect of changing to the full two-dimensional likelihood, $dN/dzdq$ (Eq. 1) in Sect. 6.2. For this purpose we compare constraints on the total matter density, $\Omega_{\rm m}$, and the linear-theory amplitude of the density perturbations today, σ_8, using the cluster counts in combination with external data and fixing the mass bias.

The two-dimensional likelihood $dN/dzdq$ is then adopted as the baseline in the rest of the paper. We extract constraints on $\Omega_{\rm m}$ and σ_8 from the cluster counts in combination with external data, imposing the different cluster mass scale calibrations as prior distributions on the mass bias. After comparing these new constraints to those from the CMB anisotropies in the base ΛCDM model (Sect. 6.3), we move to joint analysis of the cluster counts and CMB anisotropies to study, for example, extensions to the base ΛCDM model, such as non-minimal neutrino mass (Sect. 6.4). In these studies we vary all six parameters of the (flat) base ΛCDM model, except when considering model extensions for which we include the relevant parameters. Figures display contours delineating marginalized constraints.

6.1. Constraints on $\Omega_{\rm m}$ and σ_8: comparison to 2013

Figure 3 presents constraints from the MMF3 cluster counts combined with the BAO and BBN priors of Sect. 5.2; we refer to this data combination as "SZ+BAO+BBN". To compare to results from our 2013 analysis (the grey, filled ellipses), we use a one-dimensional likelihood based on Eq. (4) over the redshift distribution and have adopted the reference scaling relation of 2013, i.e., Eqs. (7) and (8) with $1 - b = 0.8$. For the present comparison, we use the updated BAO constraints discussed in Sect. 5.2; these are stronger than the BAO constraints used in the 2013 analysis, and the grey contours shown here are consequently smaller than in Planck Collaboration XX (2014).

Limiting the 2015 catalogue to $q > 8.5$ produces a sample with 190 clusters, similar to the 2013 cosmology catalogue (189 objects). The two sets of constraints demonstrate good consistency, and they remain consistent while becoming tighter as we decrease the signal-to-noise threshold of the 2015 catalogue. Under similar assumptions, our 2015 analysis thus confirms the 2013 results reported in Planck Collaboration XX (2014).

The area of the ellipse from $q = 8.5$ to $q = 6$ decreases by a factor of 1.3. This is substantially less than the factor of 2.3 expected from the ratio of the number of objects in the two samples. This difference may be related to the decreasing goodness-of-fit of the best model as the signal-to-noise decreases.

Figure 4 overlays the observed cluster redshift distribution on the predictions from the best-fit model in each case. We see that the models do not match the counts in the second and third redshift bins (counting from $z = 0$), and that the discrepancy, already marginally present at the high signal-to-noise cut corresponding to the 2013 catalogue, becomes more pronounced towards the lower signal-to-noise thresholds. This dependence on signal-to-noise may suggest that the data prefer a different slope, α, of the scaling relation than allowed by the prior of Table 1. We explore the effect of relaxing the X-ray prior on α in the next section.

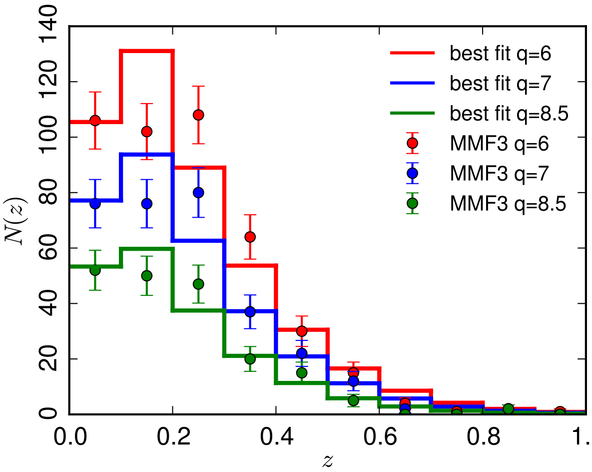

Fig. 4: Comparison of observed counts (points with error bars) with predictions of the best-fit models (solid lines) from the one-dimensional likelihood for three different thresholds applied to the 2015 MMF3 cosmology sample. The mismatch between observed and predicted counts in the second and third lowest redshift bins, already noticed in the 2013 analysis, increases at lower thresholds, q. The best-fit models are defined by the constraints shown in Fig. 3. For this figure and Fig. 3, we use our one-dimensional likelihood over the redshift distribution, dN/dz (Eq. 4).

6.2. Constraints on $\Omega_{\rm m}$ and σ_8: two-dimensional analysis

In Fig. 5 we compare constraints from the one- and two-dimensional likelihood with α either free or with the prior of Table 1. For this comparison, we continue with the "SZ+BAO+BBN" data set, but adopt the CCCP prior for the mass bias and only consider the full 2015 MMF3 catalogue at $q > 6$.

The grey and black contours and lines show results from the one-dimensional likelihood fit to the redshift distribution using, respectively, the X-ray prior on α and leaving α free. The redshift counts do indeed favour a steeper slope, and we find a posterior of $\alpha = 2.28 \pm 0.17$ in the latter case.

We define a generalized χ^2 measure of goodness-of-fit as $\chi^2 = \sum_i^{N_z} \bar{N}_i^{-1}\left(N_i - \bar{N}_i\right)^2$, determining the probability to exceed (PTE) the observed value using Monte Carlo simulations of Poisson statistics for each bin with the best-fit model mean $\bar{N}_i$. The observed value of the fit drops from 17 ($PTE = 0.07$) with the X-ray prior, to 15 ($PTE = 0.11$) when leaving α free. When leaving α free, $\Omega_{\rm m}$ increases and σ_8 decreases, following their correlation with α shown by the contours, and their uncertainty increases due to the added parameter.

The two-dimensional likelihood over $dN/dzdq$ better constrains the slope when α is free, as shown by the violet curves and contours. In this case, the preferred value drops back towards the X-ray prior: $\alpha = 1.89 \pm 0.12$, just over $1\,\sigma$ from the central X-ray value. Re-imposing the X-ray prior on α with the two-dimensional likelihood (blue curves) does little to change the parameter constraints. Although the one-dimensional likelihood prefers a steeper slope than the X-ray prior, the two-dimensional analysis does not, and the cosmological constraints remain robust to varying α.

We define a generalized χ^2 statistic as described above, now over the two-dimensional bins in the (z,q)-plane. This generalized χ^2 for the fit with the X-ray prior is 43 ($PTE = 0.28$), compared to $\chi^2 = 45$ ($PTE = 0.23$) when α is a free parameter.

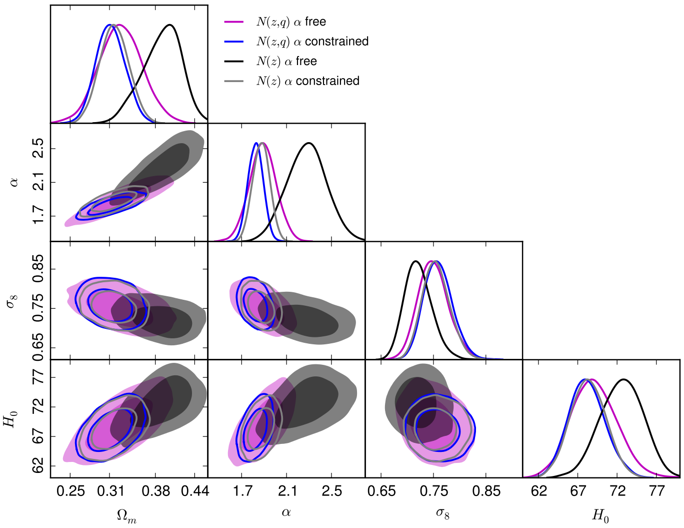

Fig. 5: Comparison of constraints from the one-dimensional (dN/dz) and two-dimensional ($dN/dzdq$) likelihoods on cosmological parameters and the scaling relation mass exponent, α. For this comparison, we adopt the CCCP prior on the mass bias and the SZ+BAO+BBN data set. The corresponding best-fit model redshift distributions are shown in Fig. 6.

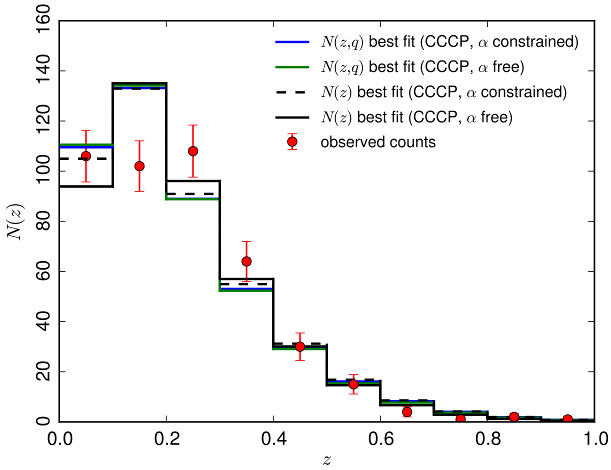

Fig. 6: Redshift distribution of best-fit models from the four analysis cases shown in Fig. 5. The observed counts in the MMF3 catalogue ($q > 6$) are plotted as the red points with error bars, and as in Fig. 5 we adopt the CCCP mass prior with the SZ+BAO+BBN data set.

Fig. 6 displays the redshift distribution of the best-fit models in all four cases. Despite their apparent difficulty in matching the second and third redshift bins, the PTE values suggest that these fits are moderately good to acceptable. Note that, as mentioned briefly in Sect. 5.1, clustering effects will increase the scatter in each bin slightly over the Poisson value we have assumed, causing our quoted PTE values to be somewhat smaller than the true ones.

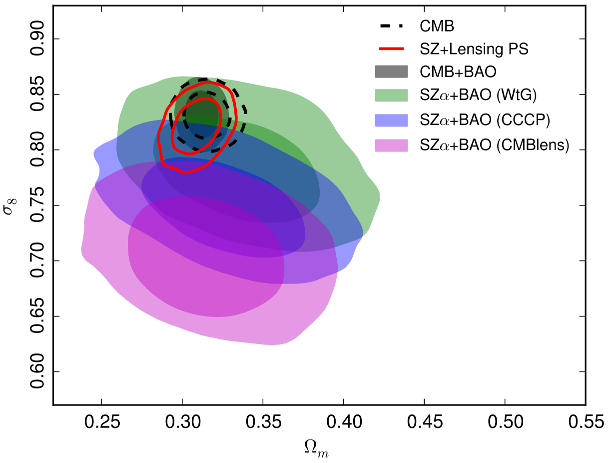

Fig. 7: Comparison of constraints from the CMB to those from the cluster counts in the $(\Omega_{\rm m}, \sigma_8)$-plane. The green, blue and violet contours give the cluster constraints (two-dimensional likelihood) at 1 and 2σ for the WtG, CCCP, and CMB lensing mass calibrations, respectively, as listed in Table 2. These constraints are obtained from the MMF3 catalogue with the SZ+BAO+BBN data set and α free. Constraints from the *Planck* TT, TE, EE+lowP CMB likelihood (hereafter, *Planck* primary CMB) are shown as the dashed contours enclosing 1 and 2σ confidence regions (Planck Collaboration XIII 2015), while the grey shaded region also include BAO. The red contours give results from a joint analysis of the cluster counts, primary CMB and the *Planck* lensing power spectrum (Planck Collaboration XV 2015), leaving the mass bias parameter free and α constrained by the X-ray prior.

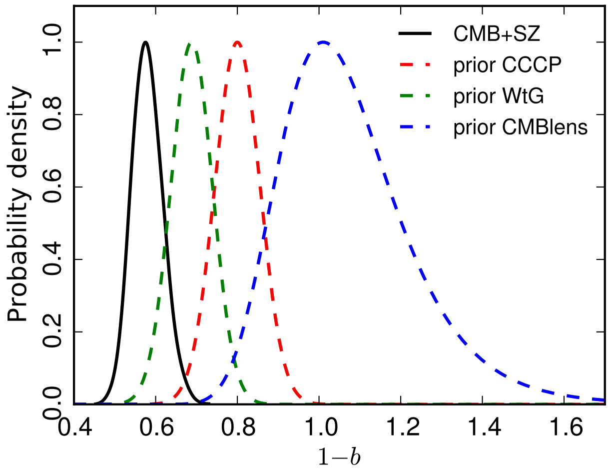

Fig. 8: Comparison of cluster and primary CMB constraints in the base ΛCDM model expressed in terms of the mass bias, $1-b$. The solid black curve shows the distribution of values required to reconcile the counts and primary CMB in ΛCDM; it is found as the posterior on the $1-b$ from a joint analysis of the *Planck* cluster counts and primary CMB when leaving the mass bias free. The coloured dashed curves show the three prior distributions on the mass bias listed in Tab. 2.

6.3. Constraints on $\Omega_{\rm m}$ and σ_8: comparison to primary CMB

Our 2013 analysis brought to light tension between constraints on $\Omega_{\rm m}$ and σ_8 from the cluster counts and those from the primary CMB in the base ΛCDM model. In that analysis, we adopted a flat prior on the mass bias over the range $1-b = [0.7, 1.0]$, with a reference model defined by $1-b = 0.8$ (see discussion in the Appendix of Planck Collaboration XX 2014). Given the good consistency between the 2013 and 2015 cluster results (Fig. 3), we expect the tension to remain under the same assumptions concerning the mass bias.

Figure 7 compares our 2015 cluster constraints (MMF3 SZ+BAO+BBN) to those for the base ΛCDM model from the *Planck* CMB anisotropies. The cluster constraints, given the three different priors on the mass bias, are shown by the filled contours at 1 and 2σ, while the dashed black contours give the *Planck* TT, TE, EE+lowP constraints (hereafter *Planck* primary CMB, Planck Collaboration XIII 2015); the grey shaded regions add BAO to the CMB. The central value of the WtG mass prior lies at the extreme end of the range used in 2013 (i.e., 1-b=0.7); with its uncertainty range extending even lower, the tension with primary CMB is greatly reduced, as pointed out by von der Linden et al. (2014b). With similar uncertainty but a central value shifted to $1-b = 0.78$, the CCCP mass prior results in greater tension with the primary CMB. The lensing mass prior, finally, implies little bias and hence much greater tension.

6.4. Joint Planck 2014 primary CMB and cluster constraints

We now turn to a joint analysis of the cluster counts and primary CMB. We begin by finding the mass bias required to remove tension with the primary CMB, and then consider one-parameter extensions to the base ΛCDM model, varying the curvature, the Thomson optical depth to reionization, the dark energy equation-of-state, and the neutrino mass scale. Unless otherwise stated, "CMB" in the following means *Planck* TT, TE, EE+lowP as defined in Planck Collaboration XIII (2015). All intervals are 68% confidence and all upper/lower limits are 95%.

6.4.1. Mass bias required by CMB

In Fig. 8 we compare the three prior distributions to the mass bias required by the primary CMB. The latter is obtained as the posterior on $(1-b)$ from a joint analysis of the MMF3 cluster counts and the CMB with the mass bias as a free parameter. The best-fit value in this case is $(1-b) = 0.58 \pm 0.04$, more than 1σ below the central WtG value. Perfect agreement with the primary CMB would imply that clusters are even more massive than the WtG calibration. This figure most clearly quantifies the tension between the *Planck* cluster counts and primary CMB.

6.4.2. Curvature

By itself the CMB only poorly determines the spatial curvature (Sect. 6.2.4 of Planck Collaboration XIII 2015), but by including another astrophysical observation, such as cluster counts, it can be tightly constrained. Our joint cluster and CMB analysis, without external data, yields $\Omega_{\rm k} = -0.012 \pm 0.008$, consistent with the constraint from *Planck* CMB and BAO $\Omega_{\rm k} = 0.000 \pm 0.002$.

6.4.3. Reionization optical depth

Primary CMB temperature anisotropies also provide a precise measurement of the parameter combination $A_{\rm s}e^{-2\tau}$, where τ is the optical depth from Thomson scatter after reionization and $A_{\rm s}$ is the power spectrum normalization on large scales (Planck Collaboration XIII 2015). Low-ℓ polarization anisotropies break the degeneracy by constraining τ, but this measurement is delicate

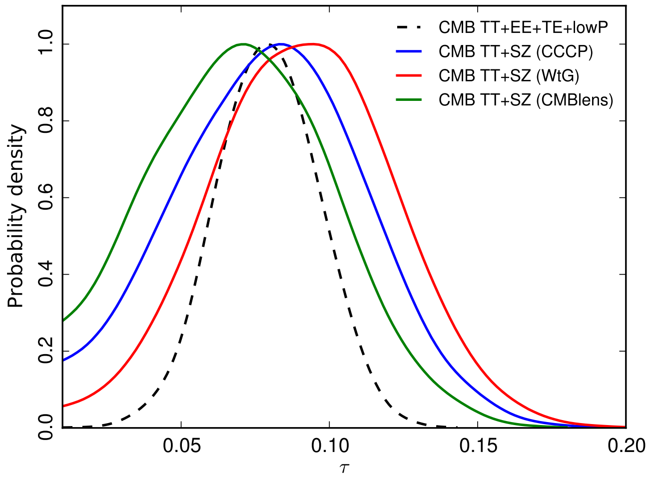

Fig. 9: Constraints on the reionization optical depth, τ. The dashed black curve is the constraint from *Planck* CMB (i.e. TT, TE, EE+lowP), while the three coloured lines are the posterior distribution on τ from a joint analysis of the cluster counts and *Planck* TT only for the three different mass bias parameters.

given the low signal amplitude and difficult systematic effects; it is important, however, in the determination of σ_8. It is therefore interesting to compare the *Planck* primary CMB constraints on τ to those from a joint analysis of the cluster counts and primary CMB without the low-ℓ polarization data (lowP). Battye et al. (2014), for instance, pointed out that a lower value for τ than suggested by WMAP could reduce the level of tension between CMB and large scale structure.

The comparison is shown in Fig. 9. We see that the *Planck* TT + SZ constraints are in good agreement with the value from *Planck* CMB (i.e., TT, TE, EE+lowP), with the preferred value for WtG slightly higher and CMB lensing pushing towards a lower value. The ordering CMB lensing/CCCP/WtG from lower to higher τ posterior values matches the decreasing level of tension with the primary CMB on σ_8. These values remain, however, larger than what is required to fully remove the tension in each case. The posterior distributions for the mass bias are $1-b = 0.60 \pm 0.042$, $1-b = 0.63 \pm 0.047$, $1-b = 0.66 \pm 0.045$, respectively, for WtG, CCCP and CMB lensing, all significantly shifted from the corresponding priors of Table 2. Allowing τ to adjust offers only minor improvement in the tension reflected by Fig. 8. Interestingly, the *Planck* TT posterior shown in Fig. 8 of Planck Collaboration XIII (2015) peaks at significantly higher values, while our *Planck* TT +SZ constraints are consistent with the constraint from *Planck* TT + lensing, an independent constraint on τ without lowP.

6.4.4. Dark energy

In Fig. 10 we examine constraints on a constant dark energy equation-of-state parameter, w. Analysis of the primary CMB alone results in highly degenerate grey contours. The degeneracy is broken by adding constraints such as BAO (blue contours) or supernovae distances (light blue contours), both picking values around $w = -1$. The SZ counts (two-dimensional likelihood with CCCP prior) only marginally break the degeneracy when combined with the CMB, but when combined with BAO they do yield interesting constraints (green contours) that are consistent with the independent constraints from the primary CMB combined with supernovae. We obtain $\Omega_m = 0.313 \pm 0.025$ and $w = -1.00 \pm 0.18$ for SZ+BAO, and $\Omega_m = 0.306 \pm 0.013$ and $w = -1.10 \pm 0.06$ for CMB+BAO.

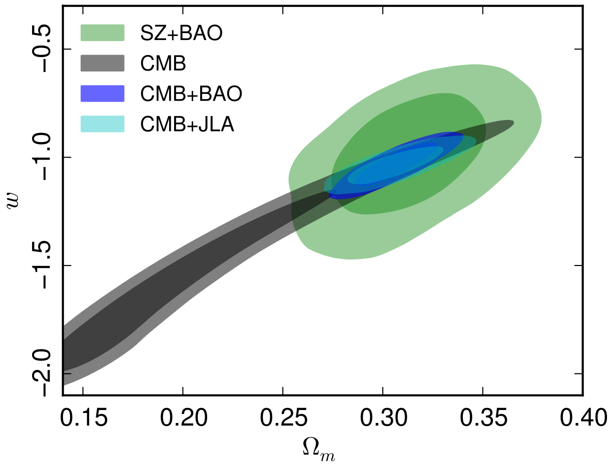

Fig. 10: Constraints on a constant dark energy equation-of-state parameter, w. Analysis of the primary CMB alone yields the grey contours that are highly degenerate. Adding either BAO or supernovae to the CMB breaks the degeneracy, giving constraints around $w = -1$. Adding SZ cluster counts from the MMF3 2015 catalogue instead to the CMB results in the rose-coloured contours. The green contours are constraints from joint analysis of the SZ counts and BAO; although much less constraining they agree with the CMB+JLA combinations and are completely independent.

6.4.5. $\sum m_\nu$

An important, well-motivated extension to the base ΛCDM model that clusters can help constrain is a non-minimal sum of neutrino masses, $\sum m_\nu > 0.06$ eV. Given the primary CMB anisotropies, the amplitude of the density perturbations today, characterized by the equivalent linear theory extrapolation, σ_8, is model dependent; it is a derived parameter depending, for example, on the composition of the matter content of the universe. Cluster abundance, on the other hand, provides a direct measurement of σ_8 at low redshifts, and comparison to the value derived from the CMB tests the adopted cosmological model.

By free-streaming, neutrinos damp the growth of matter perturbations. Our discussion thus far has assumed the minimum mass for the three known neutrino species. Increasing their mass, $\sum m_\nu > 0.06$ eV, lowers σ_8 because the neutrinos have larger gravitational influence on the total matter perturbations. This goes in the direction of reconciling tension — the strength of which depends on the mass bias — between the cluster and primary CMB constraints. Cluster abundance, or any measure of σ_8 at low redshift, is therefore an important cosmological constraint to be combined with those from the primary CMB.

Figure 11 presents a joint analysis of the cluster counts for the CCCP mass bias prior with primary CMB, the *Planck* lensing power spectrum and BAO. The results without BAO (green and red shaded contours) allow relatively large neutrino masses, up to $\sum m_\nu \sim 0.5$ eV; and when adding the lensing power spectrum, a small, broad peak appears in the posterior distribution just above $\sum m_\nu = 0.2$ eV. We also notice some interesting correlations: the amplitude, σ_8, anti-correlates with neutrino mass, as does the Hubble parameter, and larger values of α correspond to larger neutrino mass, lower H_0 and lower σ_8.

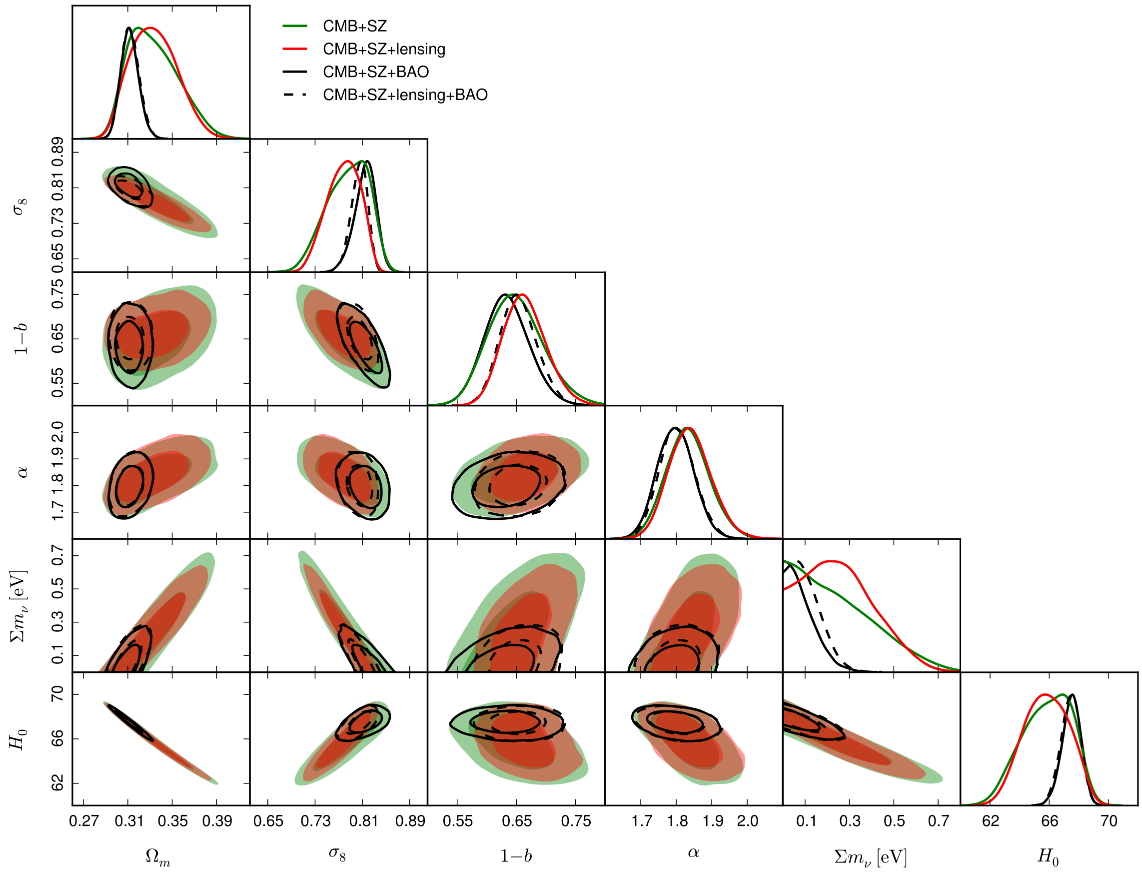

Fig. 11: Parameter constraints on the ΛCDM+non-minimal neutrino mass model. For this study, we adopt the CCCP prior on the mass bias (see Tab. 2) and leave the scaling exponent, α, free. The green and red shaded regions show, respectively, the 1 and 2σ confidence regions for joint analyses of the cluster counts using the primary CMB, and the primary CMB plus the lensing power spectrum. The solid and dashed black contours add to these two cases constraints from BAO.

As discussed in detail in Planck Collaboration XIII (2015), the anti-correlation with the Hubble parameter maintains the observed acoustic peak scale in the primary CMB. Increasing neutrino mass to simultaneously accommodate the cluster and primary CMB constraints by lowering σ_8, while allowed in this joint analysis, would therefore necessarily increase tension with some direct measurements of H_0 (see discussion in Planck Collaboration XIII (2015)). Including the BAO data greatly restricts this possibility, as shown by the solid and dashed black curves.

The solid and dashed, red and black curves in Fig. 12 reproduce the marginalized posterior distributions on $\sum m_\nu$ from Fig. 11. The solid blue curve is the result of a similar analysis where in addition the artificial parameter $A_{\rm L}$ is allowed to vary. This parameter characterizes the amount of lensing in the temperature power spectrum relative to the best fit model (Planck Collaboration XIII 2015). *Planck* TT + lowP alone constraints

$$A_{\rm L} = 1.22 \pm 0.10$$

in mild tension with the value predicted for the ΛCDM model, $A_{\rm L} = 1$. In the base ΛCDM model, this parameter is fixed to unity, but it is important to note it is degenerate with $\sum m_\nu$. Left free, it allows less lensing power, which is also in line with the direct measurement of the lensing power spectrum (labelled as Lensing PS) from the four-point function (see Planck Collaboration XIII 2015). In that light, we see that adding $A_{\rm L}$ as a free parameter accentuates the peak in the CMB+SZ+Lensing PS posterior. The small internal tension between CMB+SZ and CMB+SZ+$A_{\rm L}$ posteriors may point towards a need for an extension of the minimal six-parameter ΛCDM.

These posteriors lead to the following constraints: $\sum m_\nu < 0.53\,{\rm eV}$ (95%) for CMB+SZ+Lensing PS and $\sum m_\nu < 0.22\,{\rm eV}$ (95%) for CMB+SZ+BAO.

We may compare these with the constraints from the primary CMB presented in Planck Collaboration XIII (2015). The *Planck* primary CMB by itself places an upper limit of $\sum m_\nu < 0.49\,{\rm eV}$ (95%), and the addition of BAO tightens this to $\sum m_\nu < 0.17\,{\rm eV}$ (95%). Addition of the *Planck* lensing power spectrum to the primary CMB weakens the constraint to $\sum m_\nu < 0.59\,{\rm eV}$ (95%), as we would expect given the results and discussion above. The final constraint adopted by Planck Collaboration XIII (2015), for its robustness to possible remaining low level systematics in the polarization data, is $\sum m_\nu < 0.23\,{\rm eV}$ (95%), not too different from the peak suggested in CMB+SZ+lensing PS posterior.

Adding neutrino mass should lower σ_8, letting it move towards values favoured by the cluster counts. We might expect that the CMB+SZ combination would therefore find clear evidence for non-minimal neutrino mass. In spite of this, the green curve only places an upper limit on $\sum m_\nu$. We may understand this by looking at the posterior on the mass bias $1-b$. The allowed values are well separated from the prior distribution, meaning that the primary CMB has sufficient statistical weight to strongly override the prior. The lensing power spectrum, in favouring slightly lower σ_8, reinforces the cluster trend so that a peak appears in the posterior for $\sum m_\nu$ in the red curve; it is not

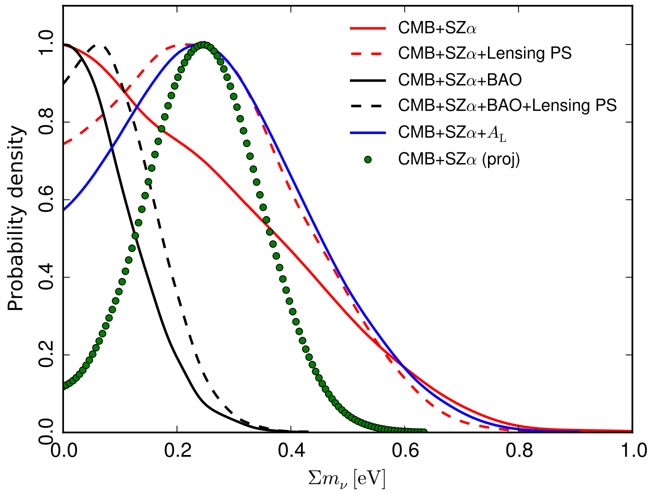

Fig. 12: Constraints on $\sum m_\nu$ from a joint analysis of the cluster counts and primary CMB. The solid and dashed, red and black lines reproduce the marginalized posterior distributions from Fig. 11. The solid blue line is the posterior from a similar analysis, but marginalized over the additional parameter A_L (see text). If applied to the present *Planck* cluster cosmology sample, a future mass calibration of $1 - b = 0.80 \pm 0.01$ would result in the bold, dotted black posterior curve.

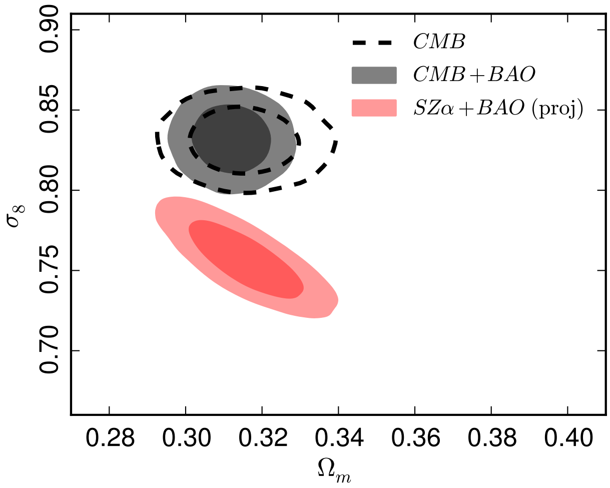

Fig. 13: Prediction of cluster constraints with a possible future mass bias prior of $1 - b = 0.80 \pm 0.01$. The black shaded region and dashed contours reproduce the current primary CMB and primary CMB+BAO constraints from *Planck* for the base ΛCDM model. The red shaded contours present the constraints expected from this mass bias prior applied to the present *Planck* cluster cosmology sample with the SZ+BAO+BBN data set.

enough, however, to bring the posterior on the mass bias in line with the prior. This indicates that the tension between the cluster and primary CMB constraints is not fully resolved.

One may then ask, how tight must the prior on the mass bias be to make a difference? To address this question, we performed an analysis assuming a projected tighter prior constraint on the mass bias. The informal target precision for cluster mass calibration with future large lensing surveys, such as *Euclid* and the Large Synoptic Survey Telescope, is 1%, and we consider the impact of a prior of $1 - b = 0.80 \pm 0.01$ on the present *Planck* cluster cosmology sample in Figs. 12 and 13.

The latter figure compares the constraints from cluster counts for this mass bias to the present primary CMB constraints in the (Ω_m, σ_8)-plane for the base ΛCDM model. The bold, black dotted curve in Fig. 12 shows the predicted posterior on the neutrino mass from a joint analysis of the present *Planck* cluster counts and primary CMB. The same prior on a much larger catalogue would demonstrate a corresponding increase in sensitivity to neutrino mass. This simple projection highlights the importance and value of the more precise cluster cosmology expected in the future, and it provides clear motivation for significant effort in mass calibration. This effort will continue with larger samples of clusters with gravitational shear measurements, and also with the new technique of CMB lensing cluster mass measurements.

7. Summary and discussion

Our 2015 analysis incorporates a number of improvements and new information relative to our first study in Planck Collaboration XX (2014). With more data, we have a larger cluster cosmology sample, increased by more than a factor of two, and we implement a two-dimensional likelihood over the counts in both redshift and signal-to-noise. We have also performed new tests of the selection function using MCXC and SPT cluster catalogs as truth tables. The selection function from these external checks and internal simulations of the *Planck* catalogue construction agree with each other and can be reasonably modelled by a simple analytical expression derived by assuming noise is the dominant factor (see the Appendix). One possible systematic effect that warrants further study is IR emission from cluster member galaxies. Finally, we have examined the implications of three recent determinations of the cluster mass bias parameter, $1 - b$. The two-dimensional likelihood with the 2015 catalogue and mass bias priors will be implemented in CosmoMC.

Our analysis confirms the results of the 2013 study. The counts are consistent with those of 2013, illustrated by the agreement in the constraints on Ω_m and σ_8 when using the same SZ observable-mass relations (see Fig. 3). The gain in statistical precision is less than expected from the larger catalogue, which is likely related to the fact that the fit to the redshift distribution with the X-ray prior on α is only marginal. Our new two-dimensional approach yields consistent, but more robust constraints than the one-dimensional likelihood over just the redshift distribution; it is less sensitive to the slope of the scaling relation, α, and it provides a better fit to the counts than in the one-dimensional case.

Using the two-dimensional likelihood as our baseline, we extracted new cosmological constraints using three different cluster mass scales represented by the mass bias prior distributions given in Table 2. The first two come from galaxy shear observations of samples of *Planck* clusters. They differ by about 1σ, with the WtG result favoring larger mass bias. We have also implemented a novel method for measuring cluster masses based lensing of the CMB temperature anisotropies behind clusters (Melin & Bartlett 2014). It gives a mass bias averaged over the entire cluster cosmology sample, although with larger statistical uncertainty.

As a new method requiring further exploration, we consider CMB lensing less robust at present than galaxy lensing mass measurements, but highly promising. Similar CMB-based mass measurements have recently been published by SPT (Baxter et al. 2014) and ACT (Madhavacheril et al. 2014). The approach is appealing because it is subject to different systematic effects than gravitational shear and because it can be applied to large cluster samples thanks to the extensive sky coverage of the CMB experiments, with *Planck* of course covering the entire sky. Gravitational shear surveys will soon attain large sky coverage in the near future with the Dark Energy Survey (DES), and in the more distant future with the *Euclid* and WFIRST space missions and the Large Synoptic Survey Telescope.

Our central result from analysis of the 2015 *Planck* cluster counts is shown in Fig. 7. Depending on the mass bias prior, we find varying degrees of tension with the primary CMB, as in 2013. The mass bias required to bring the cluster counts and CMB into full agreement is larger than indicated by any of the three priors and corresponds to $1 - b = 0.58 \pm 0.04$. Fig. 8 illustrates the situation. The WtG prior almost eliminates the tension, but not quite, while both the CCCP and CMB lensing priors remain in noticeable tension. Our largest source of modelling uncertain is, as in 2013, the mass bias.

Tension between low redshift determinations of σ_8 and the *Planck* primary CMB are not unique to the *Planck* cluster counts. Among SZ cluster surveys, both SPT and ACT are in broad agreement with our findings, the latter depending on which SZ-mass scaling relation is used, as detailed in our 2013 analysis Planck Collaboration XX (2014). And the new SPT cosmological analysis (Bocquet et al. 2014) shows a significant shift between the cluster mass scale determined from the velocity dispersion or Y_X and what is needed to satisfy *Planck* or WMAP9 CMB constraints (e.g., Fig. 2 Bocquet et al. 2014). In a study of the REFLEX X-ray luminosity function, Böhringer et al. (2014) also report general agreement with our cluster findings. On the other hand, Mantz et al. (2014) find the their X-ray cluster counts, when using the WtG mass calibration, match the primary CMB constraints.

The situation is thus not yet satisfactory. It is unclear if these modest tensions arise from low-level systematics in the astrophysical studies, or are the first glimpse of something more important. The most obvious extension to the base ΛCDM model that could in principle reconcile the differences is a non-minimal sum of neutrino masses. This, unfortunately, does not provide such a straightforward solution. While it is true that adding neutrino mass does lower σ_8 relative to the base ΛCDM prediction from the primary CMB, it does so at the the cost of increasing tension in other parameters; for example, it lowers *Planck*'s already rather low value for the Hubble parameter.

Figure 14 highlights these points by showing constraints in the (Ω_m, σ_8)- and the (H_0, σ_8)-planes for each of the mass bias parameters. Adding variable neutrino mass relaxes constraints from the primary CMB (shaded contours, which are the same in all three pairs of panels) towards lower σ_8, but by simultaneously increasing Ω_m and decreasing H_0. The remaining tension is mild in the case of the WtG mass prior, but more pronounced for the other two mass priors regardless of the neutrino mass.

Another possibility is that baryonic physics influences the late-time evolution of the density perturbations. Strong feedback from active galactic nuclei (AGN) (Nagai et al. 2007; van Daalen et al. 2011; Martizzi et al. 2014) can potentially damp growth and lower σ_8 through expulsion of matter from dark matter halos. This same effect could also reduce the mass of cluster halos and hence the prediction for their abundance, which is based on dark matter only simulations. It does not appear, however, that these effects are sufficiently large to explain the tension between low redshift and primary CMB constraints hinted at by the different observations. In addition, the violent feedback necessary for important impact might be difficult to reconcile with observations of the baryon content of dark matter halos (e.g., Planck Collaboration Int. XI 2013).

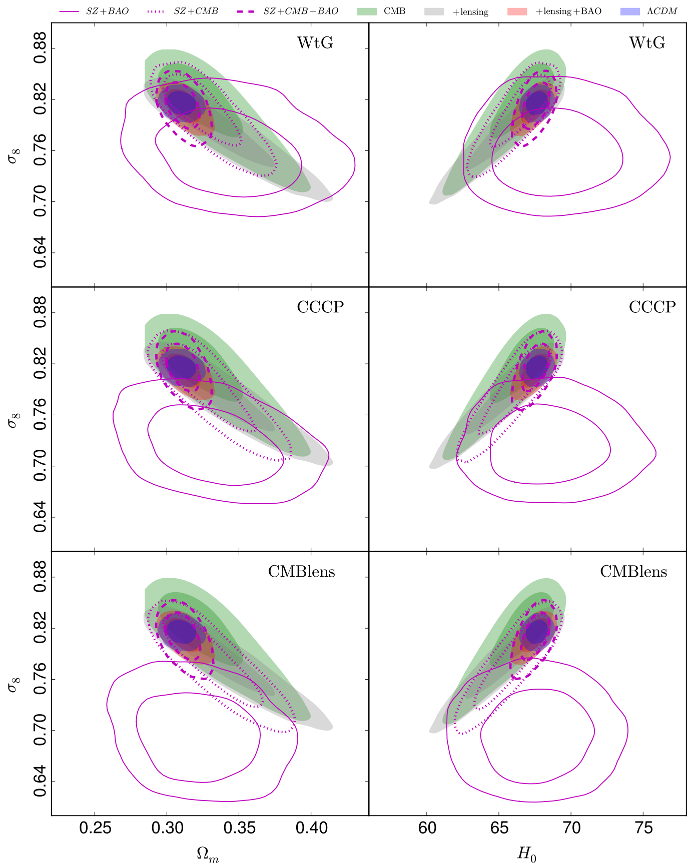

Fig. 14: Effects of neutrino mass. The open magenta contours (solid, dashed and dotted) reproduce our cluster constraints with different data combinations for the base ΛCDM (i.e., $\sum m_\nu = 0.06\,\mathrm{eV}$). The violet shaded contours trace the constraints on the base ΛCDM model, while the other shaded regions give constraints from the primary CMB combined with lensing and BAO when adding and marginalizing over variable neutrino mass.

As conclusion, we return to the main uncertainty in interpretation of the cluster counts, namely the mass bias. It could be argued that the current accuracy is at the level of $\sim 10 - 15\%$, based on the difference between different analyses and somewhat larger than their quoted statistical uncertainties. Progress will certainly follow with improvement in these measurements. We illustrate the potential impact of a 1% determination of the mass bias in Figs. 12 and 13. Such a result would, depending on the central value, significantly clarify the extent of any tensions and possible necessity for extensions to the base ΛCDM model. This precision is the avowed target of the large lensing surveys, such as *Euclid*, WFIRST and LSST. In the shorter term, we may expect valuable movement in this direction from DES and CMB lensing cluster mass measurements.

Acknowledgements. The Planck Collaboration acknowledges the support of: ESA; CNES and CNRS/INSU-IN2P3-INP (France); ASI, CNR, and INAF (Italy); NASA and DoE (USA); STFC and UKSA (UK); CSIC, MINECO, JA, and RES (Spain); Tekes, AoF, and CSC (Finland); DLR and MPG (Germany); CSA (Canada); DTU Space (Denmark); SER/SSO (Switzerland); RCN (Norway); SFI (Ireland); FCT/MCTES (Portugal); ERC and PRACE (EU). A description of the Planck Collaboration and a list of its members, indicating which technical or scientific activities they have been involved in, can be found at `http://www.cosmos.esa.int/web/planck/planck-collaboration`.

References

Anderson, L., Aubourg, É., Bailey, S., et al. 2014, MNRAS, 441, 24
Anderson, L., Aubourg, E., Bailey, S., et al. 2012, MNRAS, 427, 3435
Angulo, R. E., Springel, V., White, S. D. M., et al. 2012, MNRAS, 426, 2046
Arnaud, M., Pratt, G. W., Piffaretti, R., et al. 2010, A&A, 517, A92
Arnaud et al., i. p. 2015
Battye, R. A., Charnock, T., & Moss, A. 2014, ArXiv e-prints
Baxter, E. J., Keisler, R., Dodelson, S., et al. 2014, ArXiv e-prints
Becker, M. R. & Kravtsov, A. V. 2011, ApJ, 740, 25
Benson, B. A., de Haan, T., Dudley, J. P., et al. 2013, ApJ, 763, 147
Bersanelli, M., Mandolesi, N., Butler, R. C., et al. 2010, A&A, 520, A4
Betoule, M., Kessler, R., Guy, J., et al. 2014, A&A, 568, A22
Beutler, F., Blake, C., Colless, M., et al. 2011, MNRAS, 416, 3017
Bleem, L. E., Stalder, B., de Haan, T., et al. 2014, ArXiv e-prints
Bocquet, S., Saro, A., Mohr, J. J., et al. 2014, ArXiv e-prints
Böhringer, H., Chon, G., & Collins, C. A. 2014, A&A, 570, A31
Carlstrom, J. E., Ade, P. A. R., Aird, K. A., et al. 2011, PASP, 123, 568
Carvalho, P., Rocha, G., & Hobson, M. P. 2009, MNRAS, 393, 681
Chamballu, A., Bartlett, J. G., & Melin, J.-B. 2012, A&A, 544, A40
Hasselfield, M., Hilton, M., Marriage, T. A., et al. 2013, J. Cosmology Astropart. Phys., 7, 8
Hoekstra et al., i. p. 2015
Hu, W. & Kravtsov, A. V. 2003, ApJ, 584, 702
Lamarre, J., Puget, J., Ade, P. A. R., et al. 2010, A&A, 520, A9
Lewis, A. & Challinor, A. 2006, Phys. Rep., 429, 1
Madhavacheril, M., Sehgal, N., Allison, R., et al. 2014, ArXiv e-prints
Mantz, A. B., von der Linden, A., Allen, S. W., et al. 2014, ArXiv e-prints
Marrone, D. P., Smith, G. P., Okabe, N., et al. 2012, ApJ, 754, 119
Martizzi, D., Mohammed, I., Teyssier, R., & Moore, B. 2014, MNRAS, 440, 2290
Melin, J., Bartlett, J. G., & Delabrouille, J. 2006, A&A, 459, 341
Melin, J.-B. & Bartlett, J. G. 2014
Meneghetti, M., Rasia, E., Merten, J., et al. 2010, A&A, 514, A93
Mennella, A., Butler, R. C., Curto, A., et al. 2011, A&A, 536, A3
Merten, J., Meneghetti, M., Postman, M., et al. 2014, ArXiv e-prints
Nagai, D., Kravtsov, A. V., & Vikhlinin, A. 2007, ApJ, 668, 1
Navarro, J. F., Frenk, C. S., & White, S. D. M. 1997, ApJ, 490, 493
Padmanabhan, N., Xu, X., Eisenstein, D. J., et al. 2012, MNRAS, 427, 2132
Piffaretti, R., Arnaud, M., Pratt, G. W., Pointecouteau, E., & Melin, J.-B. 2011, A&A, 534, A109
Piffaretti, R. & Valdarnini, R. 2008, A&A, 491, 71
Planck HFI Core Team. 2011, A&A, 536, A4
Planck Collaboration I. 2011, A&A, 536, A1
Planck Collaboration I. 2014, A&A, 571, A1
Planck Collaboration XVI. 2014, A&A, 571, A16
Planck Collaboration XX. 2014, A&A, 571, A20
Planck Collaboration XXIX. 2014, A&A, 571, A29
Planck Collaboration I. 2015, in preparation
Planck Collaboration II. 2015, in preparation
Planck Collaboration III. 2015, in preparation
Planck Collaboration IV. 2015, in preparation
Planck Collaboration V. 2015, in preparation
Planck Collaboration VI. 2015, in preparation
Planck Collaboration VII. 2015, in preparation
Planck Collaboration VIII. 2015, in preparation
Planck Collaboration IX. 2015, in preparation
Planck Collaboration X. 2015, in preparation
Planck Collaboration XI. 2015, in preparation
Planck Collaboration XII. 2015, in preparation
Planck Collaboration XIII. 2015, in preparation
Planck Collaboration XIV. 2015, in preparation
Planck Collaboration XV. 2015, in preparation
Planck Collaboration XVI. 2015, in preparation
Planck Collaboration XVII. 2015, in preparation
Planck Collaboration XVIII. 2015, in preparation
Planck Collaboration XIX. 2015, in preparation
Planck Collaboration XX. 2015, in preparation
Planck Collaboration XXI. 2015, in preparation
Planck Collaboration XXII. 2015, in preparation
Planck Collaboration XXIII. 2015, in preparation
Planck Collaboration XXIV. 2015, in preparation
Planck Collaboration XXV. 2015, in preparation
Planck Collaboration XXVI. 2015, in preparation
Planck Collaboration XXVII. 2015, in preparation
Planck Collaboration XXVIII. 2015, in preparation
Planck Collaboration Int. III. 2013, A&A, 550, A129
Planck Collaboration Int. XI. 2013, A&A, 557, A52
Postman, M., Coe, D., Benítez, N., et al. 2012, ApJS, 199, 25
Reichardt, C. L., Stalder, B., Bleem, L. E., et al. 2013, ApJ, 763, 127
Rozo, E., Bartlett, J. G., Evrard, A. E., & Rykoff, E. S. 2014a, MNRAS, 438, 78
Rozo, E., Evrard, A. E., Rykoff, E. S., & Bartlett, J. G. 2014b, MNRAS, 438, 62
Rozo, E., Rykoff, E. S., Bartlett, J. G., & Evrard, A. 2014c, MNRAS, 438, 49
Steigman, G. 2008, ArXiv e-prints
Swetz, D. S., Ade, P. A. R., Amiri, M., et al. 2011, ApJS, 194, 41
Tauber, J. A., Mandolesi, N., Puget, J., et al. 2010, A&A, 520, A1
Tinker, J., Kravtsov, A. V., Klypin, A., et al. 2008, ApJ, 688, 709
Umetsu, K., Medezinski, E., Nonino, M., et al. 2014, ArXiv e-prints
van Daalen, M. P., Schaye, J., Booth, C. M., & Dalla Vecchia, C. 2011, MNRAS, 415, 3649
von der Linden, A., Allen, M. T., Applegate, D. E., et al. 2014a, MNRAS, 439, 2
von der Linden, A., Mantz, A., Allen, S. W., et al. 2014b, ArXiv e-prints
Watson, W. A., Iliev, I. T., D'Aloisio, A., et al. 2013, MNRAS, 433, 1230
Zaldarriaga, M. & Seljak, U. 1999, Phys. Rev. D, 59, 123507

---

[1] APC, AstroParticule et Cosmologie, Université Paris Diderot, CNRS/IN2P3, CEA/lrfu, Observatoire de Paris, Sorbonne Paris Cité, 10, rue Alice Domon et Léonie Duquet, 75205 Paris Cedex 13, France
[2] Aalto University Metsähovi Radio Observatory and Dept of Radio Science and Engineering, P.O. Box 13000, FI-00076 AALTO, Finland
[3] African Institute for Mathematical Sciences, 6-8 Melrose Road, Muizenberg, Cape Town, South Africa
[4] Agenzia Spaziale Italiana Science Data Center, Via del Politecnico snc, 00133, Roma, Italy
[5] Aix Marseille Université, CNRS, LAM (Laboratoire d'Astrophysique de Marseille) UMR 7326, 13388, Marseille, France
[6] Astrophysics Group, Cavendish Laboratory, University of Cambridge, J J Thomson Avenue, Cambridge CB3 0HE, U.K.
[7] Astrophysics & Cosmology Research Unit, School of Mathematics, Statistics & Computer Science, University of KwaZulu-Natal, Westville Campus, Private Bag X54001, Durban 4000, South Africa
[8] Atacama Large Millimeter/submillimeter Array, ALMA Santiago Central Offices, Alonso de Cordova 3107, Vitacura, Casilla 763 0355, Santiago, Chile
[9] CITA, University of Toronto, 60 St. George St., Toronto, ON M5S 3H8, Canada
[10] CNRS, IRAP, 9 Av. colonel Roche, BP 44346, F-31028 Toulouse cedex 4, France
[11] CRANN, Trinity College, Dublin, Ireland
[12] California Institute of Technology, Pasadena, California, U.S.A.
[13] Centre for Theoretical Cosmology, DAMTP, University of Cambridge, Wilberforce Road, Cambridge CB3 0WA, U.K.
[14] Centro de Estudios de Física del Cosmos de Aragón (CEFCA), Plaza San Juan, 1, planta 2, E-44001, Teruel, Spain
[15] Computational Cosmology Center, Lawrence Berkeley National Laboratory, Berkeley, California, U.S.A.
[16] Consejo Superior de Investigaciones Científicas (CSIC), Madrid, Spain
[17] DSM/Irfu/SPP, CEA-Saclay, F-91191 Gif-sur-Yvette Cedex, France
[18] DTU Space, National Space Institute, Technical University of Denmark, Elektrovej 327, DK-2800 Kgs. Lyngby, Denmark
[19] Département de Physique Théorique, Université de Genève, 24, Quai E. Ansermet,1211 Genève 4, Switzerland
[20] Departamento de Física, Universidad de Oviedo, Avda. Calvo Sotelo s/n, Oviedo, Spain
[21] Department of Astronomy and Astrophysics, University of Toronto, 50 Saint George Street, Toronto, Ontario, Canada
[22] Department of Astrophysics/IMAPP, Radboud University Nijmegen, P.O. Box 9010, 6500 GL Nijmegen, The Netherlands
[23] Department of Physics & Astronomy, University of British Columbia, 6224 Agricultural Road, Vancouver, British Columbia, Canada
[24] Department of Physics and Astronomy, Dana and David Dornsife College of Letter, Arts and Sciences, University of Southern California, Los Angeles, CA 90089, U.S.A.
[25] Department of Physics and Astronomy, University College London, London WC1E 6BT, U.K.

[26] Department of Physics, Florida State University, Keen Physics Building, 77 Chieftan Way, Tallahassee, Florida, U.S.A.
[27] Department of Physics, Gustaf Hällströmin katu 2a, University of Helsinki, Helsinki, Finland
[28] Department of Physics, Princeton University, Princeton, New Jersey, U.S.A.
[29] Department of Physics, University of California, Santa Barbara, California, U.S.A.
[30] Department of Physics, University of Illinois at Urbana-Champaign, 1110 West Green Street, Urbana, Illinois, U.S.A.
[31] Dipartimento di Fisica e Astronomia G. Galilei, Università degli Studi di Padova, via Marzolo 8, 35131 Padova, Italy
[32] Dipartimento di Fisica e Scienze della Terra, Università di Ferrara, Via Saragat 1, 44122 Ferrara, Italy
[33] Dipartimento di Fisica, Università La Sapienza, P. le A. Moro 2, Roma, Italy
[34] Dipartimento di Fisica, Università degli Studi di Milano, Via Celoria, 16, Milano, Italy
[35] Dipartimento di Fisica, Università degli Studi di Trieste, via A. Valerio 2, Trieste, Italy
[36] Dipartimento di Fisica, Università di Roma Tor Vergata, Via della Ricerca Scientifica, 1, Roma, Italy
[37] Dipartimento di Matematica, Università di Roma Tor Vergata, Via della Ricerca Scientifica, 1, Roma, Italy
[38] Discovery Center, Niels Bohr Institute, Blegdamsvej 17, Copenhagen, Denmark
[39] Dpto. Astrofísica, Universidad de La Laguna (ULL), E-38206 La Laguna, Tenerife, Spain
[40] European Southern Observatory, ESO Vitacura, Alonso de Cordova 3107, Vitacura, Casilla 19001, Santiago, Chile
[41] European Space Agency, ESAC, Planck Science Office, Camino bajo del Castillo, s/n, Urbanización Villafranca del Castillo, Villanueva de la Cañada, Madrid, Spain
[42] European Space Agency, ESTEC, Keplerlaan 1, 2201 AZ Noordwijk, The Netherlands
[43] Facoltà di Ingegneria, Università degli Studi e-Campus, Via Isimbardi 10, Novedrate (CO), 22060, Italy
[44] Gran Sasso Science Institute, INFN, viale F. Crispi 7, 67100 L'Aquila, Italy
[45] HGSFP and University of Heidelberg, Theoretical Physics Department, Philosophenweg 16, 69120, Heidelberg, Germany
[46] Haverford College Astronomy Department, 370 Lancaster Avenue, Haverford, Pennsylvania, U.S.A.
[47] Helsinki Institute of Physics, Gustaf Hällströmin katu 2, University of Helsinki, Helsinki, Finland
[48] INAF - Osservatorio Astrofisico di Catania, Via S. Sofia 78, Catania, Italy
[49] INAF - Osservatorio Astronomico di Padova, Vicolo dell'Osservatorio 5, Padova, Italy
[50] INAF - Osservatorio Astronomico di Roma, via di Frascati 33, Monte Porzio Catone, Italy
[51] INAF - Osservatorio Astronomico di Trieste, Via G.B. Tiepolo 11, Trieste, Italy
[52] INAF/IASF Bologna, Via Gobetti 101, Bologna, Italy
[53] INAF/IASF Milano, Via E. Bassini 15, Milano, Italy
[54] INFN, Sezione di Bologna, Via Irnerio 46, I-40126, Bologna, Italy
[55] INFN, Sezione di Roma 1, Università di Roma Sapienza, Piazzale Aldo Moro 2, 00185, Roma, Italy
[56] INFN, Sezione di Roma 2, Università di Roma Tor Vergata, Via della Ricerca Scientifica, 1, Roma, Italy
[57] INFN/National Institute for Nuclear Physics, Via Valerio 2, I-34127 Trieste, Italy
[58] IPAG: Institut de Planétologie et d'Astrophysique de Grenoble, Université Grenoble Alpes, IPAG, F-38000 Grenoble, France, CNRS, IPAG, F-38000 Grenoble, France
[59] ISDC, Department of Astronomy, University of Geneva, ch. d'Ecogia 16, 1290 Versoix, Switzerland
[60] IUCAA, Post Bag 4, Ganeshkhind, Pune University Campus, Pune 411 007, India
[61] Imperial College London, Astrophysics group, Blackett Laboratory, Prince Consort Road, London, SW7 2AZ, U.K.
[62] Infrared Processing and Analysis Center, California Institute of Technology, Pasadena, CA 91125, U.S.A.
[63] Institut Néel, CNRS, Université Joseph Fourier Grenoble I, 25 rue des Martyrs, Grenoble, France
[64] Institut Universitaire de France, 103, bd Saint-Michel, 75005, Paris, France
[65] Institut d'Astrophysique Spatiale, CNRS (UMR8617) Université Paris-Sud 11, Bâtiment 121, Orsay, France
[66] Institut d'Astrophysique de Paris, CNRS (UMR7095), 98 bis Boulevard Arago, F-75014, Paris, France
[67] Institute for Space Sciences, Bucharest-Magurale, Romania
[68] Institute of Astronomy, University of Cambridge, Madingley Road, Cambridge CB3 0HA, U.K.
[69] Institute of Theoretical Astrophysics, University of Oslo, Blindern, Oslo, Norway
[70] Instituto de Astrofísica de Canarias, C/Vía Láctea s/n, La Laguna, Tenerife, Spain
[71] Instituto de Física de Cantabria (CSIC-Universidad de Cantabria), Avda. de los Castros s/n, Santander, Spain
[72] Istituto Nazionale di Fisica Nucleare, Sezione di Padova, via Marzolo 8, I-35131 Padova, Italy
[73] Jet Propulsion Laboratory, California Institute of Technology, 4800 Oak Grove Drive, Pasadena, California, U.S.A.
[74] Jodrell Bank Centre for Astrophysics, Alan Turing Building, School of Physics and Astronomy, The University of Manchester, Oxford Road, Manchester, M13 9PL, U.K.
[75] Kavli Institute for Cosmology Cambridge, Madingley Road, Cambridge, CB3 0HA, U.K.
[76] LAL, Université Paris-Sud, CNRS/IN2P3, Orsay, France
[77] LAPTh, Univ. de Savoie, CNRS, B.P.110, Annecy-le-Vieux F-74941, France
[78] LERMA, CNRS, Observatoire de Paris, 61 Avenue de l'Observatoire, Paris, France
[79] Laboratoire AIM, IRFU/Service d'Astrophysique - CEA/DSM - CNRS - Université Paris Diderot, Bât. 709, CEA-Saclay, F-91191 Gif-sur-Yvette Cedex, France
[80] Laboratoire Traitement et Communication de l'Information, CNRS (UMR 5141) and Télécom ParisTech, 46 rue Barrault F-75634 Paris Cedex 13, France
[81] Laboratoire de Physique Subatomique et Cosmologie, Université Grenoble-Alpes, CNRS/IN2P3, 53, rue des Martyrs, 38026 Grenoble Cedex, France
[82] Laboratoire de Physique Théorique, Université Paris-Sud 11 & CNRS, Bâtiment 210, 91405 Orsay, France
[83] Lawrence Berkeley National Laboratory, Berkeley, California, U.S.A.
[84] Lebedev Physical Institute of the Russian Academy of Sciences, Astro Space Centre, 84/32 Profsoyuznaya st., Moscow, GSP-7, 117997, Russia
[85] Max-Planck-Institut für Astrophysik, Karl-Schwarzschild-Str. 1, 85741 Garching, Germany
[86] McGill Physics, Ernest Rutherford Physics Building, McGill University, 3600 rue University, Montréal, QC, H3A 2T8, Canada
[87] National University of Ireland, Department of Experimental Physics, Maynooth, Co. Kildare, Ireland
[88] Niels Bohr Institute, Blegdamsvej 17, Copenhagen, Denmark
[89] Optical Science Laboratory, University College London, Gower Street, London, U.K.
[90] SB-ITP-LPPC, EPFL, CH-1015, Lausanne, Switzerland
[91] SISSA, Astrophysics Sector, via Bonomea 265, 34136, Trieste, Italy
[92] School of Physics and Astronomy, Cardiff University, Queens Buildings, The Parade, Cardiff, CF24 3AA, U.K.
[93] School of Physics and Astronomy, University of Nottingham, Nottingham NG7 2RD, U.K.
[94] Sorbonne Université-UPMC, UMR7095, Institut d'Astrophysique de Paris, 98 bis Boulevard Arago, F-75014, Paris, France

[95] Space Research Institute (IKI), Russian Academy of Sciences, Profsoyuznaya Str, 84/32, Moscow, 117997, Russia
[96] Space Sciences Laboratory, University of California, Berkeley, California, U.S.A.
[97] Special Astrophysical Observatory, Russian Academy of Sciences, Nizhnij Arkhyz, Zelenchukskiy region, Karachai-Cherkessian Republic, 369167, Russia
[98] Stanford University, Dept of Physics, Varian Physics Bldg, 382 Via Pueblo Mall, Stanford, California, U.S.A.
[99] Sub-Department of Astrophysics, University of Oxford, Keble Road, Oxford OX1 3RH, U.K.
[100] Theory Division, PH-TH, CERN, CH-1211, Geneva 23, Switzerland
[101] UPMC Univ Paris 06, UMR7095, 98 bis Boulevard Arago, F-75014, Paris, France
[102] Université de Toulouse, UPS-OMP, IRAP, F-31028 Toulouse cedex 4, France
[103] University Observatory, Ludwig Maximilian University of Munich, Scheinerstrasse 1, 81679 Munich, Germany
[104] University of Granada, Departamento de Física Teórica y del Cosmos, Facultad de Ciencias, Granada, Spain
[105] University of Granada, Instituto Carlos I de Física Teórica y Computacional, Granada, Spain
[106] Warsaw University Observatory, Aleje Ujazdowskie 4, 00-478 Warszawa, Poland

Appendix A: Modelling uncertainties

We examine the robustness of our cosmological constraints to modelling uncertainties. We first consider sensitivity to the cosmological sample and to our modelling of the completeness function in Sect. A.1, and then look at the effect of using a different mass function in Sec. A.2. In Sec. A.3, we show that our constraints are robust against redshift evolution of the scaling relations.

Appendix A.1: Choice of the sample and selection function

For our baseline analysis, we use the MMF3 cosmological sample and its associated completeness based on the analytical approximation using the Error Function (Eq. 14). In Fig. A.1 we show how the Monte Carlo determined selection function changes the cosmological constraints (labelled QA for "Quality Assessment" in the figure). We also present the constraints obtained from the intersection sample defined in Sec. 2. The figure is based on the 1D $N(z)$ likelihood, for which the Monte Carlo completeness can be easily computed, and we use the baseline SZ+BAO+BBN data set and fix $(1-b) = 0.8$. The MMF3 ERF contour is thus close to the $q = 6$ contour of Fig. 3, the only difference being that $\sigma_{\ln Y}$ is fixed to zero in Fig. A.1. while it is constrained by the Table 1 prior in Fig. 3. The impact of adopting the intersection sample and/or the QA completeness function is small ($< 0.5\sigma$) for both $\Omega_{\rm m}$ and σ_8.

Appendix A.2: Mass function

We use the Tinker et al. mass function for our baseline analysis. To characterize the influence of this choice, we examine constraints when adopting the mass function from Watson et al. (2013) instead. We employ our 2D $N(z,q)$ likelihood (with the CCCP mass bias prior and α constrained) and combine with BAO and BBN prior constraints, and show the result in Fig. A.2. The Tinker et al. contour of Fig. A.2 is thus identical to the $N(z,q)$ contour with α free, as given in Fig. 5. The new mass function shifts our constraints by about 1σ towards higher $\Omega_{\rm m}$ and lower σ_8, along the main degeneracy line, hence increasing the tension with the *Planck* primary CMB constraints. Note that we use the general fit from Eq. (12) of Watson et al. (2013) (independent of redshift). This was not the case for our 2013 paper (Planck Collaboration XX 2014) where we adopted the AHF fit with parameters varying with redshift in the first ArXiv version of the paper, which was subsequently found to be incorrect (fourth version of the paper on ArXiv).

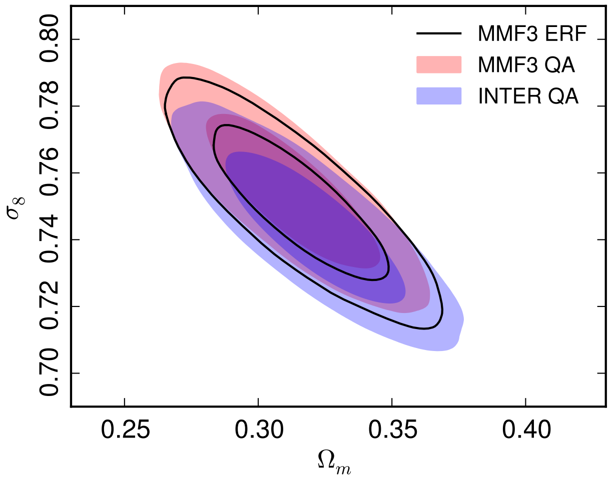

Fig. A.1: Robustness to the choice of cluster sample and the selection function model. The shaded contours give the cosmological constraints from the 2015 MMF3 cluster catalogue using the analytical (Error Function, ERF) selection function model (grey), the MMF3 Monte Carlo selection function (red), and the Monte Carlo selection function for the intersection sample (blue). Our final constraints are obtained from the MMF3 ERF model. For this comparison, we adopt the SZ+BAO+BBN data set and we fix $(1-b) = 0.8$.

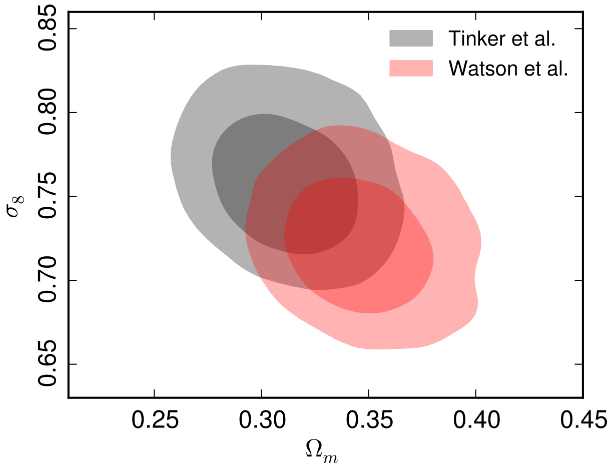

Fig. A.2: Robustness to the choice of mass function. The grey shaded contours give the cosmological constraints when using the Tinker et al. mass function, corresponding to our final result. This is compared to constraints obtained when using the Watson et al. mass function, shown as the red shaded contours. In this figure we adopt the SZ+BAO+BBN data set and the CCCP mass bias prior.

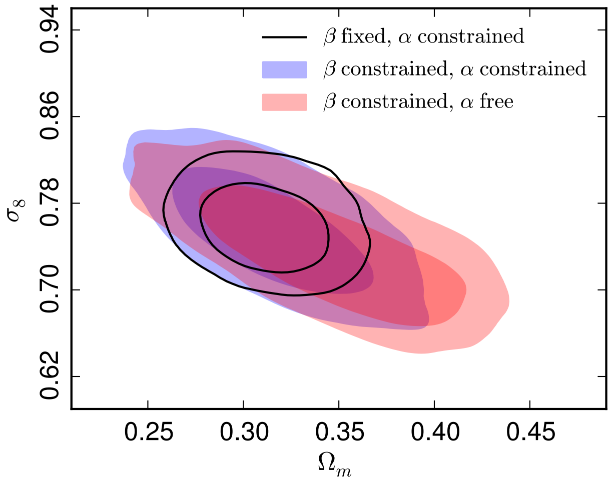

Fig. A.3: Robustness to redshift evolution in the SZ-mass scaling relation. The different contours show the constraints when relaxing the redshift evolution exponent, β, of Eq. (7). The black contours result from fixing $\beta = 0.66$, our fiducial value throughout, with α constrained by the Gaussian X-ray prior of Tab. 1. Applying a Gaussian the prior on β instead, from Tab. 1, produces the blue contours, while the red contours result when we also leave α free. In this figure we adopt the SZ+BAO+BBN data set and the CCCP mass bias prior.

Appendix A.3: Redshift evolution of the Y-M relation

Throughout our baseline analysis, we fix the redshift evolution exponent $\beta = 0.66$ (self-similar prediction) in Eq. (7). Here we examine the impact of allowing this parameter to vary. Constraints when leaving β free are shown in Fig. A.3. The "β fixed, α constrained" case corresponds to the 2D $N(z, q)$ likelihood (CCCP mass bias prior and α constrained) combined with BAO and BBN, as in Fig. A.2. This contour is also identical to the $N(z, q)$ contour with α free, shown in Fig. 5. For the "β constrained" cases, β is allowed to vary over the range 0.66 ± 0.50 (Table 1). This increases the size of our constraints along the major degeneracy between Ω_m and σ_8, but does not bring them into any closer agreement with the primary CMB.